Photovoltaic Characterization of Porphyrin and Porphyrin-Fullerene Electropolymers

by

James W. Bridgewater

A Dissertation Presented in Partial Fulfillment
of the Requirement for the Degree
Doctor of Philosophy

Approved April 2014 by the
Graduate Supervisory Committee:

Devens Gust, Co-Chair
Nongjian Tao, Co-Chair
Ian Gould
Rodolfo Diaz
Dieter K. Schroder

ARIZONA STATE UNIVERSITY

May 2014

ABSTRACT

Wide spread adoption of photovoltaic technology is limited by cost. Developing photovoltaics based on low-cost materials and processing techniques is one strategy for reducing the cost of electricity generated by photovoltaics. With this in mind, novel porphyrin and porphyrin-fullerene electropolymers have been developed here at Arizona State University. Porphyrins are attractive for inclusion in the light absorbing layer of photovoltaics due to their high absorption coefficients (on the order of 10^5 cm^{-1}) and porphyrin-fullerene dyads are attractive for use in photovoltaics due to their ability to produce ultrafast photoinduced charge separation (on the order of 10^{-15} s). The focus of this thesis is the characterization of the photovoltaic properties of these electropolymer films. Films formed on transparent conductive oxide (TCO) substrates were contacted using a mercury drop electrode in order to measure photocurrent spectra and current-voltage curves. Surface treatment of both the TCO substrate and the mercury drop is shown to have a dramatic effect on the photovoltaic performance of the electropolymer films. Treating the TCO substrates with chlorotrimethylsilane and the mercury drop with hexanethiol was found to produce an optimal tradeoff between photocurrent and photovoltage. Incident photon to current efficiency spectra of the films show that the dominant photocurrent generation mechanism in this system is located at the polymer-mercury interface. The optical field intensity at this interface approaches zero due to interference from the light reflected by the mercury surface. Reliance upon photocurrent generation at this interface limits the performance of this system and suggests that these polymers may be useful in solar cells which have structures optimized to take advantage of their internal optical field distributions.

ACKNOWLEDGEMENTS

I have learned a great deal from many different people in my time at Arizona State University. First and foremost I would like to thank my advisor, Devens Gust, for his willingness to accept a graduate student from outside his own discipline. I have benefited tremendously from our time together.

So numerous are the helpful members of the research group led by Devens Gust, Tom Moore, and Ana Moore that I will not attempt to name them all here, but will mention just one. I cannot overstate the value of the assistance I received from Paul Liddell who synthesized the monomers used to make the polymers described herein and always made the time to answer chemistry questions for an electrical engineer working in the chemistry lab.

I would also like to thank Ian Gould and Dieter K. Schroder for their outstanding instruction which I had the pleasure of experiencing first hand. Dr. Gould's excellent organic chemistry classes taught me the quantum mechanical foundations of chemical bonding in addition to providing the concepts and terminology required to communicate with my peers in the chemistry lab. The semiconductor device theory class taught by the late Dr. Schroder showed me just how clear and intuitive this challenging subject can be in the hands of an expert instructor.

Finally, I must thank all of the members of my graduate committee for the valuable feedback they supplied on this work.

TABLE OF CONTENTS

CHAPTER Page

LIST OF TABLES

LIST OF FIGURES

Figure Page

Figure Page

Figure Page

Figure Page

Figure Page

Chapter 1

INTRODUCTION AND BACKGROUND

1.1 Motivation, The Need for Renewable Energy

The United States Energy Information Administration's International Energy Outlook 2013 projects that global electricity production will grow by 93% between 2010 and 2040 (IEO, 2013). It also predicts that renewables and nuclear power will be the fastest growing energy sources during this period because of concerns about the environmental impact of fossil fuels, concerns about energy security, and sustained high oil prices. Nevertheless electricity generation from fossil fuels is projected to grow due to increased demand for electricity and insufficient supplies of competitively priced renewable alternatives. Most of the growth in renewable electricity generation is expected to come from hydroelectric and wind generation, which are cost competitive with fossil fuels, rather than electricity generated using photovoltaics. However, potential growth of hydroelectric generation in developed countries is limited because most of the resources that are economical to develop have already been exploited, therefore most renewable capacity growth in developed countries comes from wind and solar (IEO, 2013). The power output from a wind turbine or a photovoltaic panel depends upon the weather and cannot be increased in order to match demand. Renewable energy sources that vary with the weather like wind and solar are referred to as variable renewables. Power plants that can adjust their output to match demand like hydroelectric, nuclear, and fossil fuel plants are referred to as dispacthable plants. Flexible resources like dispatchable power plants and energy storage facilities are required to compensate for the variations in power output from variable renewables. A

2011 report by the International Energy Agency suggests that the United States has enough flexible resources to accommodate up to 45% of total electricity generation from variable renewables (HVR, 2011), however, in 2012 wind and solar accounted for just 3.5% of total electricity generation in the US (USE, 2012).

Combining wind and solar electricity generation reduces total output variability (Jacobson and Delucchi, 2010). However, while electricity generated from wind is cost competitive with electricity generated from fossil fuels, the cost of electricity from a new photovoltaic power plant is more than twice as expensive as electricity from a new natural gas power plant (AEO, 2013). One approach to reducing the cost of solar electricity is to develop photovoltaics based on low-cost carbon based polymer semiconductors that can be deposited with mass production friendly techniques like spin-coating or electropolymerization. The strong visible light absorption of porphyrins make them appealing for inclusion in the light absorbing layer of photovoltaic devices. With this in mind two novel porphyrin electropolymers have been developed here at Arizona State University (Liddell *et al.*, 2008; Gervaldo *et al.*, 2010). Electropolymerization in these novel porphyrin polymers takes place through the porphyrin macrocycle. In previously reported porphyrin polymers polymerization takes place through substituents and the porphyrin is merely a spectator (Li *et al.*, 2005; Poriel *et al.*, 2005; Duanmu *et al.*, 2004; Wöhrle, 2000; Bedioui *et al.*, 1995; Fish *et al.*, 1992; Basu and Rohatgi-Mukherjee, 1991). Films of these novel porphyrin electropolymers were formed on fluorine-doped tin oxide (FTO) substrates by oxidative electropolymerization. The polymerization process in these novel polymers suggests strong electronic coupling between the porphyrin macrocycle and the underlying substrate which should aid in the extraction of photoexcited carriers. The characterization of the photovoltaic properties of these polymers is the subject of this work.

1.2 Photovoltaic Concepts and Terminology

1.2.1 Current Density–Voltage Curves

The parameters measured to evaluate the performance of a solar cell include the open-circuit voltage, Voc, the short-circuit current density, Jsc, the fill factor, FF, and the power conversion efficiency, PCE. The J-V curve in Figure 1.1 illustrates these concepts. The open-circuit voltage is the maximum voltage the cell can produce and the short-circuit current density is the maximum current the cell can produce divided by the area of the cell. Pmax in Figure 1.1 is the maximum power output of the cell divided by the area of the cell. The fill factor is the ratio of the areas of the two rectangles in the figure. The area of the smaller rectangle, drawn with solid lines, is Pmax and the area of the bigger rectangle, drawn with dashed lines, is the product of Jsc and Voc. For high power conversion efficiency, the fill factor should be as close to one as possible. Record efficiency solar cells have fill factors between 0.6 and 0.9 (Green *et al.*, 2014). The most important performance metric for a solar cell is its power conversion efficiency. The power conversion efficiency is Pmax divided by the power available from the light source per unit area.

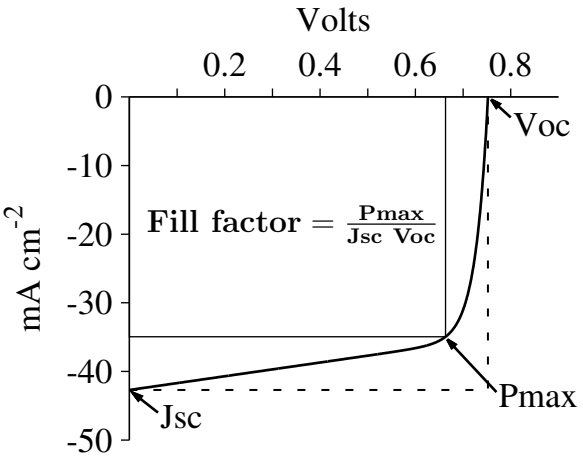

Figure 1.1: J-V curve illustrating solar cell performance metrics.

1.2.2 Incident Photon to Current Efficiency

Photocurrent density spectra can be helpful in determining what process is limiting cell performance, however as measured these spectra contain features from the spectrum of the light source as well as features from the cell. The features from the light source can be removed by normalizing the results by the light intensity at each wavelength. A particulary useful way to do this is to express the current density in units of electrons per second per unit area and express the light intensity in units of photons per second per unit area. When expressed in these units, the ratio of current density to light intensity reveals what fraction of photons incident upon the cell produced an electron in the photocurrent and is known as both external quantum efficiency (EQE) and incident photon to current efficiency (IPCE). Figure 1.2 illustrates how IPCE is calculated from the current density measured when the cell is illuminated with monochromatic light of known intensity. In the equation in Figure 1.2, h is Planck's constant, c is the speed of light, q is the charge of an electron, and λ is the wavelength of the monochromatic light.

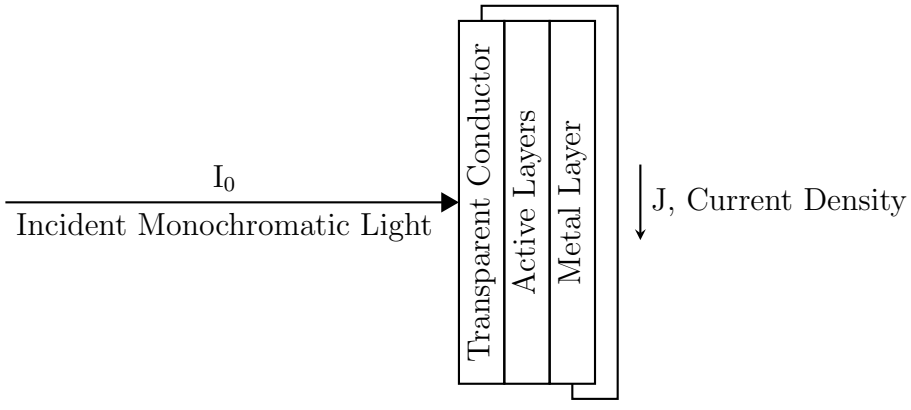

$$\text{IPCE} = \frac{\text{Number of electrons in the current}}{\text{Number of photons in the light}} = \frac{J}{I_0} \times \frac{hc}{q\lambda}$$

Figure 1.2: Illustration of short-circuit current density measurement under monochromatic light. At each wavelength, IPCE is calculated from the photocurrent density and light intensity.

1.2.3 Light Harvesting Efficiency

Light harvesting efficiency (LHE) is calculated from absorbance, A, as shown in Figure 1.3. Light harvesting efficiency is also know as the fraction of light absorbed. The IPCE of a solar cell is limited by the fraction of incident photons that the cell absorbs, therefore IPCE spectra are compared with light harvesting efficiency spectra rather than light absorption spectra.

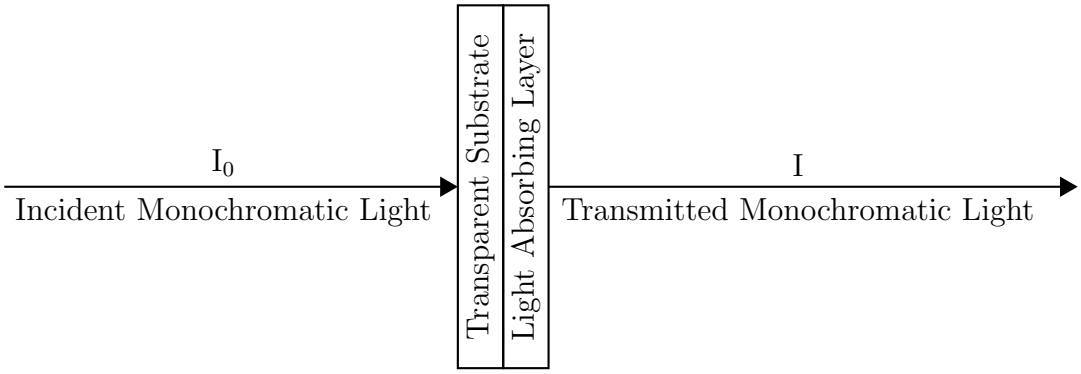

$$\text{LHE} = \text{fraction of light absorbed} = 1 - \frac{I}{I_0} = 1 - 10^{-A}$$

Figure 1.3: Illustration of monochromatic light absorption measurement. Light harvesting efficiency is calculated from absorbance at each wavelength.

1.2.4 The Solar Spectrum

ASTM International (formerly The American Society for Testing and Materials) maintains standard solar spectra that are used in the evaluation of photovoltaic cells (AST, 2012). There are three spectra: extraterrestrial, direct, and global. The extraterrestrial spectrum is the total solar irradiance just outside the earth's atmosphere, the direct spectrum is the direct solar irradiance at sea level, and the global spectrum is the total irradiance at sea level and includes both direct and diffuse light. These three spectra are known as AM0, AM1.5D, and AM1.5G respectively. AM (air mass) refers to specific atmospheric conditions and 1.5 refers to the distance the light

travels through the atmosphere. Light in the AM1.5D and AM1.5G spectra travels a distance through air that is 1.5 times the thickness of the earth's atmosphere. These spectra were originally intended to be representative of the average solar intensity in the continental United States. For the evaluation of terrestrial solar cells that do not employ solar concentrators, AM1.5G is the spectrum of interest. This spectrum is shown in Figure 1.4.

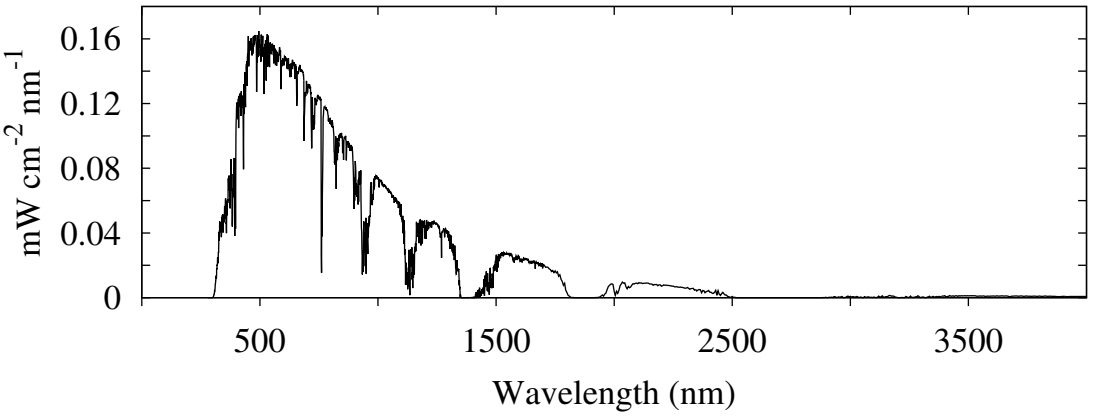

Figure 1.4: Spectral irradiance of ASTM International's AM1.5G solar spectrum standard (AST, 2012).

The intensity of the AM1.5G spectrum is about 100 mW/cm^2 and for the purposes of photovoltaic testing it is frequently normalized to this value. This makes it easy to estimate the power conversion efficiency of a solar cell from its maximum power in mW/cm^2. A cell that produces 10 mW/cm^2 under AM1.5G light with a total intensity of 100 mW/cm^2 has a power conversion efficiency of 10%.

1.3 Photovoltaic Performance Limits

In 1961 Shockley and Queisser published the seminal work on the theoretical power conversion efficiency limits of photovoltaics that utilize a single light absorbing material (Shockley and Queisser, 1961). They postulate three unavoidable loss

mechanisms. The first is the failure of the light absorbing material to absorb photons with energies below its optical bandgap. The second is the loss of energy that exceeds the optical bandgap which occurs because photoexcited electrons thermally relax to the lowest excited state prior to being collected at the photoanode. These two loss mechanisms alone reduce the maximum efficiency of single light absorber photovoltaics under AM1.5G light to just under 50%. The third loss mechanism is radiative emission. All materials radiate light in a temperature dependent manner as described by Planck's law so there is radiative emission from all solar cells. When a solar cell is in thermal equilibrium its radiative emission is simply its black body radiation. For a light absorbing material with a bandgap E_g, the number of photons it emits per second per unit area is given by Equation 1.1.

$$\Phi_{cell}(E_g) = \frac{2\pi}{h^3c^2}\int_{E_g}^{\infty}\frac{E^2}{e^{E/kT}-1}dE \tag{1.1}$$

The rate of radiative recombination in a semiconducting material is proportional to the product of the electron concentration, n, and the hole-concentration, p. When a semiconductor is in thermal equilibrium $np = n_i^2$ where n_i is its intrinsic carrier concentration. A solar cell in thermal equilibrium with a surface area A_{cell} has a radiative recombination rate of $2A_{cell}\Phi_{cell}$ where the factor of two arises because cells radiate from both their front and rear sides. Under illumination $np > n_i^2$ and the radiative recombination rate increases by the factor np/n_i^2 as seen in Equation 1.2.

$$R_{rad}(E_g) = 2A_{cell}\Phi_{cell}(E_g)\frac{np}{n_i^2} \tag{1.2}$$

A solar cell under illumination separates excess charge carriers. Positive charge carriers go to the positive terminal and negative charge carriers go to the negative terminal. These excess carriers change the chemical potential in the semiconductor and create two quasi-Fermi levels, one near the negative terminal, E_{fn}, and one near

the positive terminal, E_{fp}. The relationships below relate the carrier concentrations to these quasi-Fermi levels.

$$n = n_i e^{(E_{fn}-E_i)/kT} \tag{1.3}$$

$$p = n_i e^{(E_i-E_{fp})/kT} \tag{1.4}$$

Using these expressions to calculate np and recognizing that the difference between these two quasi-Fermi levels is the output voltage of the cell times the electronic charge results in Equation 1.5 which provides the product of the free carrier concentrations as a function of voltage.

$$np = n_i^2 e^{(E_{fn}-E_{fp})/kT} = n_i^2 e^{qV/kT} \tag{1.5}$$

The recombination rate from Equation 1.2 can be used to calculate the corresponding current density by multiplying it by the electronic charge, q. Substituting the results from Equation 1.5 for np produces Equation 1.6 which gives the radiative recombination current density as a function of cell voltage.

$$J_{rad}(Eg, V) = 2q\Phi_{cell}(E_g)\frac{np}{n_i^2} = 2q\Phi_{cell}(E_g)e^{qV/kT} \tag{1.6}$$

1.3.1 Current Density Limit

The maximum short-circuit current density of a solar cell illuminated by AM1.5G light is limited by the first and third loss mechanisms listed above, the failure to absorb photons with energies less than the bandgap and radiative emission. Figure 1.5 shows the spectral photon flux, $\phi_{AM1.5G}$, of the AM1.5G spectrum. The current density corresponding to absorption of all photons above the bandgap energy, E_g, can be found by integrating this spectrum from E_g to ∞ and multiplying the result by the electronic charge, q, as shown in Equation 1.7. Subtracting the current density from radiative recombination at zero potential results in the maximum short-circuit

photocurrent density, J_{max}, in Equation 1.8.

$$J_{AM1.5G}(E_g) = q \int_{E_g}^{\infty} \phi_{AM1.5G}(E) dE \tag{1.7}$$

$$J_{max}(E_g) = J_{AM1.5G}(E_g) - J_{rad}(E_g, 0) \tag{1.8}$$

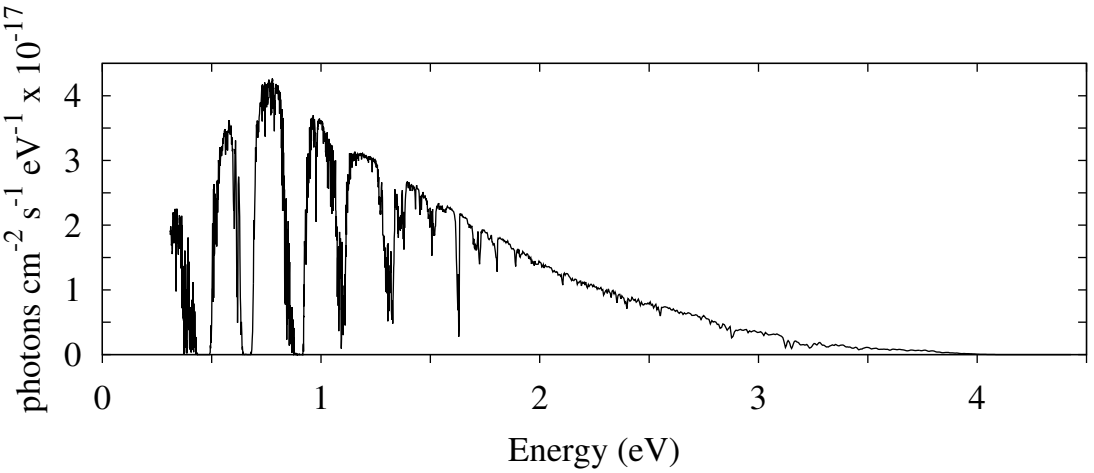

Figure 1.5: Spectral photon flux of ASTM International's AM1.5G solar spectrum standard (AST, 2012).

Performing this calculation for all bandgap energy values present in the spectrum produces the maximum current density vs bandgap energy graph in Figure 1.6. An ideal solar cell that absorbs all photons in the AM1.5G spectrum would produce a short-circuit current density around 68.5 mA/cm^2. An ideal silicon solar cell with a bandgap of 1.1 eV would produce a short-circuit current density of just over 44 mA/cm^2.

1.3.2 Voltage Limit

For an ideal solar cell that has only radiative recombination, the maximum voltage the cell can produce is the voltage at which the rate of radiative recombination is equal to the rate at which light absorption generates electron-hole pairs. Setting J_{rad} from Equation 1.6 equal to $J_{AM1.5G}$ from Equation 1.7 and solving for V produces

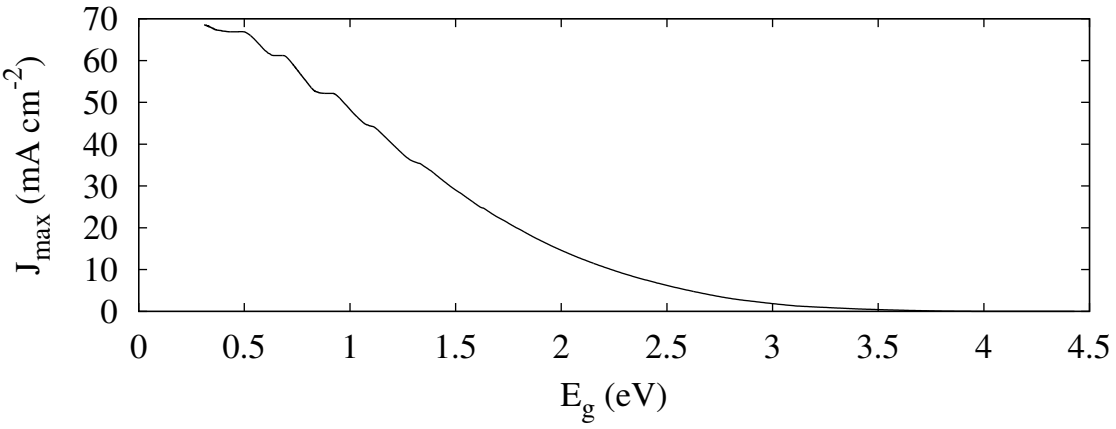

Figure 1.6: Maximum current density vs bandgap for cells under AM1.5G light.

Equation 1.9 for the maximum open-circuit voltage, V_{max}.

$$V_{max}(E_g) = \frac{kT}{q} log\left(\frac{J_{AM1.5G}(E_g)}{2q\Phi_{cell}(E_g)}\right) \tag{1.9}$$

Figure 1.7(a) shows the maximum voltage for all possible values of the bandgap energy calculated using Equation 1.9. The maximum voltage falls off for bandgaps above four electron volts because the AM1.5G spectrum contains very few photons with this much energy as seen in Figure 1.5. Dividing the maximum voltage by its corresponding bandgap energy shows that the maximum voltage is between 75 and 85% of the bandgap energy for bandgaps between 1 eV and 2 eV as seen in Figure 1.7(b). The maximum open-circuit voltage for an ideal silicon solar cell with a bandgap of 1.1 eV is 0.84 V.

1.3.3 Power Conversion Efficiency Limit

The photocurrent density for an ideal cell with only radiative recombination can be found by subtracting the voltage dependent recombination current density from the maximum current density possible under AM1.5G illumination as shown in Equa-

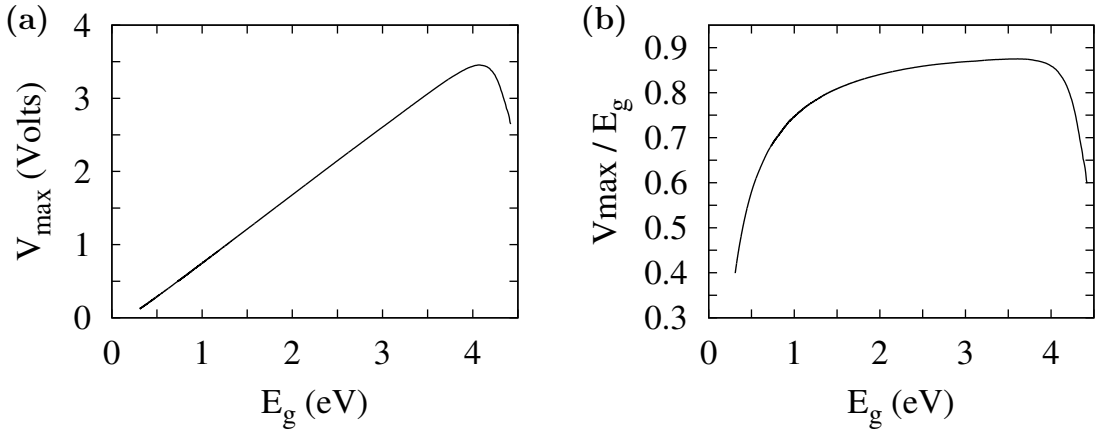

Figure 1.7: Maximum voltage vs bandgap (a) and maximum voltage divided by bandgap vs bandgap (b) under AM1.5G light.

tion 1.10.

$$J_{photo}(E_g, V) = J_{AM1.5G}(E_g) - J_{rad}(E_g, V) \tag{1.10}$$

Using Equation 1.10 to find the maximum power density for all bandgap values and using these power density values to calculate the power conversion efficiencies gives the maximum theoretical power conversion efficiencies in Figure 1.8. Maximum efficiencies are nearly the same for bandgap energies between 1.1 and 1.5 eV, around 32%.

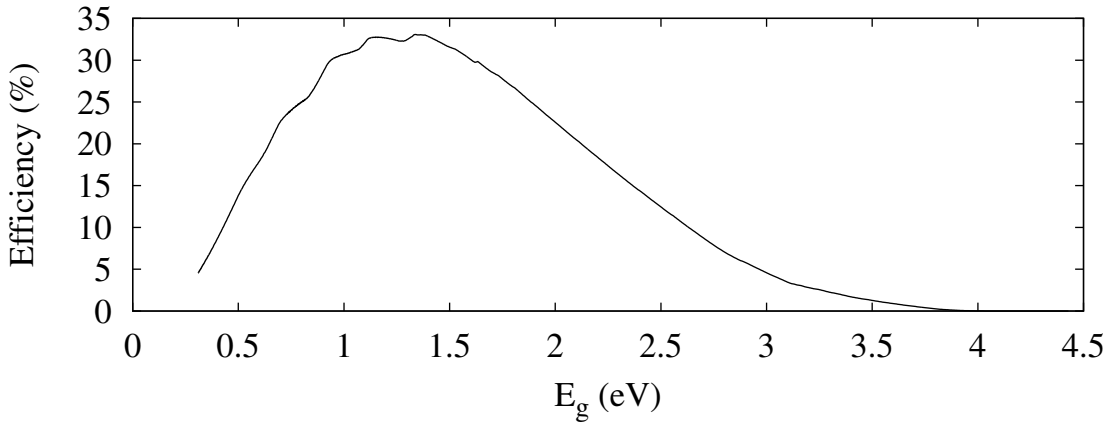

Figure 1.8: Power conversion efficiency vs bandgap for cells under AM1.5G light.

1.4 How Conventional Solar Cells Work

Conventional solar cells are made from wafers of single crystal silicon or thin-films of multicrystaline materials such as cadmium-telluride (CdTe) and copper-indium-galium-diselenide (CIGS). Impurities are introduced into these materials at precise concentrations in a process known as doping to enable the formation of regions that have an excess of electrons in the conduction band (n-type regions) and regions that have an excess of vacant orbitals in the valence band (p-type regions). When a p-type region is formed next to an n-type region electrons from the n-type region fill some of the vacancies in the valence band of the p-type region. This exchange of electrons results in the formation of an electric field at the interface between the two regions and the resulting structure is referred to as a p-n junction. This electric field is responsible for the band bending seen in the energy band diagrams of p-n junctions like the one shown in Figure 1.9. Conventional solar cells utilize the electric field at p-n junctions to separate negatively charged photoexcited electrons in the conduction band from the positively charged vacancies that they left behind in the valence band.

When the device is illuminated, this built-in electric field separates the photoexcited carriers by pushing electrons towards the n-type region and holes towards the p-type region. These excess photogenerated carriers cause the splitting of the equilibrium Fermi level into two quasi-Fermi levels. The output voltage of a p-n junction solar cell is the difference between these quasi-Fermi levels, E_{fn} and E_{fp}, in Figure 1.9 which shows energy band diagrams of a p-n junction for both short-circuit and open-circuit conditions.

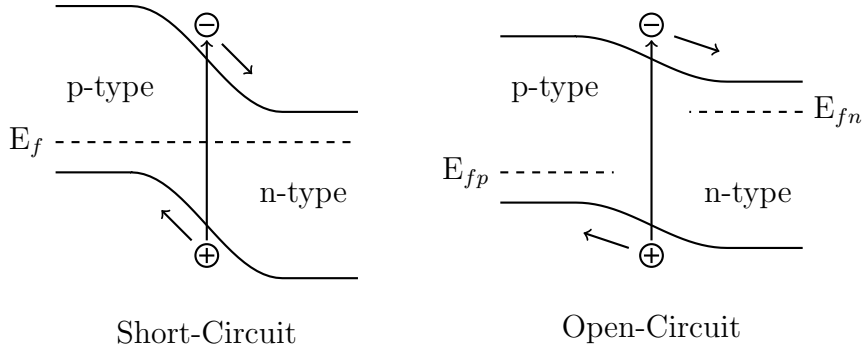

Figure 1.9: Energy band diagrams of a conventional p-n junction solar cell.

1.5 A Brief Review of Organic Photovoltaics

1.5.1 Single Layer Cells

The successful construction of an organic photovoltaic junction was reported in 1958 (Kearns and Calvin, 1958), not long after the report of an inorganic photovoltaic cell made at Bell Labs and reports of semiconducting behavior in organic materials. Although the cell in this report was constructed of two layers of different organic materials, an arrangement that would provide a breakthrough in carrier separation efficiency almost 30 years later, most early reports involved a single organic material sandwiched between two metal contacts. In organic semiconductors, absorption of photons produces excited states that are strongly localized on individual molecules or polymer chains (Hains *et al.*, 2010). These localized excited states are commonly referred to as Frenkel excitons, or simply excitons, in the literature relevant to organic photovoltaics. The conceptual basis for the observation of the photovoltaic effect in single layer organic devices is the injection of the photoexcited electron from the molecule on which it is localized into the photoanode. This process is referred to as exciton dissociation. The resulting radical cation must be reduced by a neigboring molecule and this process repeated until a radical cation is formed at and reduced

by the photocathode. This process is known as hole diffusion. In single-layer organic solar cells, the dissociation of photogenerated excitons is attributed to an electric field in the organic semiconductor caused by the difference in work functions between the two metal contacts. When a metal and a semiconductor are brought into contact, charge is transferred between them until their Fermi levels are brought into alignment. This charge transfer creates an electric field at the interface and the resulting potential barrier is called a Schottky barrier. In hole-conducting organic semiconductors, the Schottky barrier is greatest at the interface between the semiconductor and the lower work function metal due to the large difference between the Fermi levels of these two materials. Figure 1.10 shows the energy band diagram of a photovoltaic cell made by placing a hole-conducting organic semiconductor between indium tin oxide (ITO) and aluminum. Aluminum is the low work function metal in this cell. The electric field at the semiconductor-aluminum interface exerts forces on photogenerated excitons that results in electron injection into the aluminum and hole drift away from the aluminum.

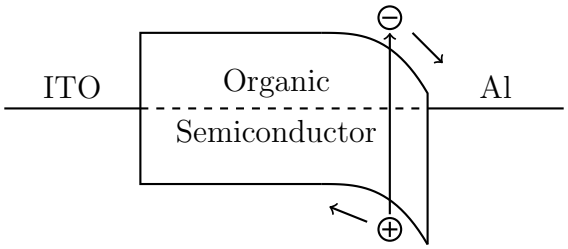

Figure 1.10: Short-circuit energy band diagram of a single layer organic solar cell.

Experiments with devices of this type have shown that their spectral photocurrent response is proportional to the fraction of light absorbed by the organic semiconductor when illuminated from the low work function side and is not proportional to the fraction of light absorbed by the organic semiconductor when illuminated from the high work function side (Tang and Albrecht, 1975). These responses are called sym-

batic and antibatic respectively. Exciting the device at wavelengths where the organic layer has the strongest absorption produces excitons that are close to the illuminated surface. The fact that these wavelengths produce more photocurrent when illuminating the device from the low work function side than they do when illuminating the device from the high work function side demonstrates that exciton dissociation is more efficient near the interface with the low work function metal. When this type of cell is illuminated from the high work function side, thick semiconductor films only serve to reduce the number of photons that are absorbed at the low work function side. The highest power conversion efficiency reported for a single layer cell was 0.7% (Morel *et al.*, 1978). This cell utilized a merocyanine dye as the organic semiconductor and was illuminated from the low work function side through a semi-transparent aluminum contact.

1.5.2 Bilayer Heterojunctions

A breakthrough in the efficiency of charge separation was made by Tang who reported a two layer organic cell in 1986 (Tang, 1986). This cell consisted of layers of a copper phthalocyanine (CuPc), a perylene derivative (PV), and silver (Ag) all thermally evaporated on indium tin oxide (ITO) as shown in Figure 1.11.

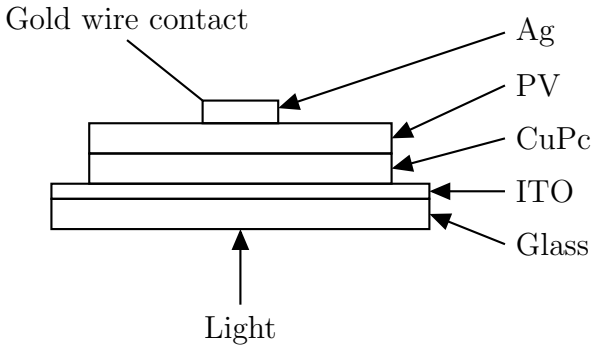

Figure 1.11: Illustration of Tang's 1986 bilayer organic photovoltaic cell.

Due to the different energetics of copper phthalocyanines and perylenes, the transfer of photoexcited electrons from the copper phthalocyanine to the perylene is energetically favorable. Becuase of this, the copper phthalocyanine is referred to as an electron donor and the perylene is referred to as an electron acceptor. The energetics of this donor-acceptor system are shown in Figure 1.12.

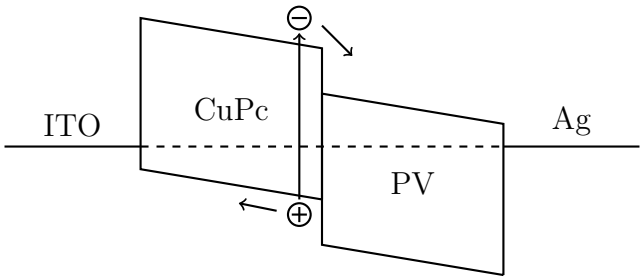

Figure 1.12: Short-circuit energy band diagram of Tang's bilayer cell.

This cell's power conversion efficiency of 1% is substantially better than most single layer cells and it exhibited two other remarkable improvements over previous reports. The first improvement was that its fill factor of 0.65 is substantially better than that of single layer devices which have fill factors around 0.25. The second improvement exhibited by this cell is that, unlike single layer cells, its photocurrent was not substantially increased by applying a reverse bias potential indicating that the cell was inherently efficient at dissociating photogenerated excitons.

Another interesting feature of this cell is that the observed open-circuit voltage was insensitive to the choice of metal for the back contact. Indium, copper, aluminum, and silver were each used and the open-circuit voltages of these cells were all within 50 mV of one another. This cell would have produced an even more substantial improvement in efficiency were it not for its low open-circuit voltage. Unlike single layer devices, the difference in work functions between the contacts is not what determines the open-circuit voltage of heterojunction cells. Subsequent studies of factors influencing the open-circuit voltage of heterojunction cells have demonstrated that the open-circuit

voltage is linearly dependent on both the LUMO of the acceptor (Brabec *et al.*, 2001) and the HOMO of the donor (Scharber *et al.*, 2006).

Despite the improvements that bilayer heterojunctions achieved, their external quantum efficiencies are much less than unity. Their low quantum efficiencies suggest that the exciton diffusion length in the organic semiconductor is less than the optical absorption length (Halls *et al.*, 1996). The measured values of exciton diffusion lengths in poly(p-phenylene vinylene) derivatives and polythiophene derivatives are between 4 and 20 nm (Haugeneder *et al.*, 1999; Savenije *et al.*, 1998; Theander *et al.*, 2000; Pettersson *et al.*, 1999). Figure 1.13 shows the molecular structures of three compounds that have been used in organic heterojunctions. MEH-PPV and P3HT are polymers that have been used as the electron donor and PCBM is a C_{60} derivative that has been used as the electron acceptor. The names of these compounds are: poly[2-methoxy-5-(2-ethylhexyloxy)-1,4-phenylenevinylene], poly(3-hexylthiophene), and phenyl-C_{61}-butyric acid methyl ester.

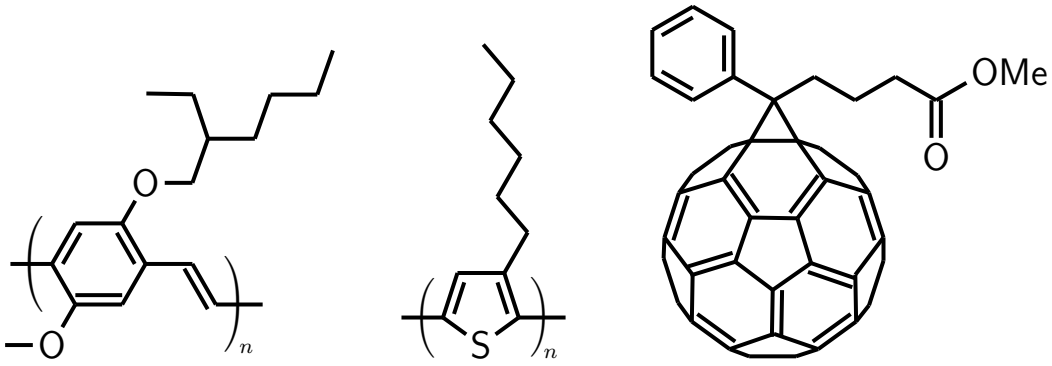

MEH-PPV P3HT PCBM

Figure 1.13: Molecular structures of MEH-PPV, P3HT, and PCBM.

1.5.3 Bulk Heterojunctions

To address the exciton diffusion length limitation, researchers began using active layers of interpenetrating donor-acceptor networks (Halls *et al.*, 1995; Yu and Heeger, 1995). This type of cell is known as a bulk heterojunction and is illustrated in Figure 1.14 where the grey and black represent regions of donor and acceptor materials.

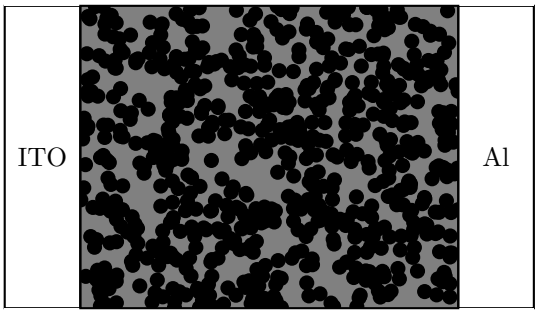

Figure 1.14: Illustration of a donor-acceptor bulk heterojunction solar cell.

In bulk heterojunctions, the donor and acceptor phases are intimately mixed. When this mixing is achieved on the proper length scale, it creates a situation in which most excitons are formed within an exciton diffusion length of a donor-acceptor interface. This is accomplished by spin-casting a mixture containing both the donor and acceptor onto the substrate. The donor and acceptor domain sizes in the spin-cast film are affected by the choice of solvent and post-deposition annealing is frequently used to optimize performance (Shaheen *et al.*, 2001; Padinger *et al.*, 2003). Bulk heterojunction cells utilizing P3HT as the electron donating material and PCBM as the electron accepting material have achieved efficiencies near 5% (Kim *et al.*, 2006; Reyes-Reyes *et al.*, 2005).

1.5.4 Interfacial Layers

Additional device layers are required to achieve good performance in bulk heterojunction cells. The active layer in a bulk heterojunction has no inherent asymmetry and charge carriers diffuse towards both metal interfaces. To achieve high efficiency, the photoanode interface must be selective for electrons and the photocathode interface must be selective for holes. The first report of a 5% efficient P3HT:PCBM bulk heterojunction (Reyes-Reyes *et al.*, 2005) utilized poly(3,4-ethylenedioxythiophene)-:poly(styrenesulfonate), or PEDOT:PSS, to increase the effective work function of ITO, improving its alignment with the donor HOMO and thereby increasing the selectivity for holes at the photocathode (Carter *et al.*, 1997). This device also used lithium fluoride at the photoanode to decrease the effective work function of aluminum, improving alignment with the acceptor LUMO and increasing selectivity for electrons (Hung *et al.*, 1997).

Wide bandgap semiconductors can also be used as interfacial layers. A carefully chosen wide-band semiconductor can be used to block transport of holes while allowing transport of electrons or vice versa. One report of a 5% efficient bulk heterojunction cell used an amorphous titanium oxide layer at the anode interface (Kim *et al.*, 2006). The HOMO of this amorphous titanium oxide is much lower than that of P3HT and PCBM which prevents hole injection into the photoanode and the LUMO of this material is lower than that of PCBM which allows electron injection. The energetics of this cell are shown in Figure 1.15.

1.5.5 Optical Interference

There was another benefit to using this titanium oxide layer at the rear interface in this cell. The active layers in this cell must be kept thin due to their limited charge

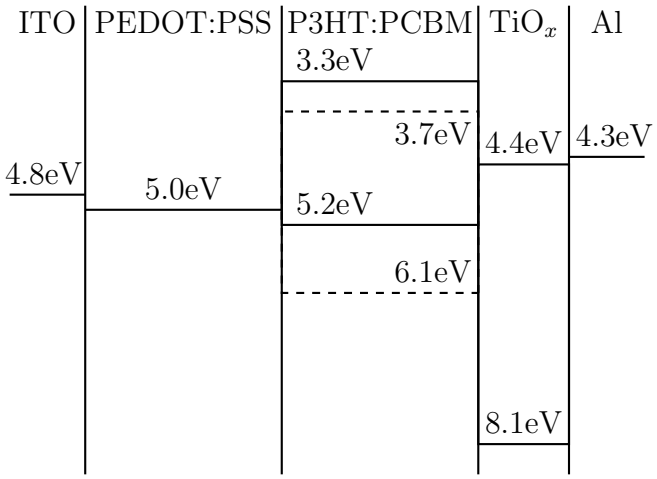

Figure 1.15: Energy level diagram of a bulk heterojunction cell with a TiO_x hole blocking layer (Kim *et al.*, 2006).

carrier mobilities and as a result of this not all of the incident light is absorbed, some of it reaches the rear interface where it is reflected off of the aluminum surface. This reflected light wave interferes with the incident light thereby producing a standing wave of light intensity inside the cell as illustrated in Figure 1.5.5. Positioning the active layer to coincide with a maximum in the standing wave of light intensity inside the device is important for maximizing light absorption in the active layer. Electromagnetic waves attenuate very quickly inside metals so the light intensity will approach zero near the aluminum interface. The titanium oxide layer in this cell served to move the active layer of the device away from the rear contact where the light intensity approaches zero to the location of a maximum in the standing wave of light intensity (Kim *et al.*, 2006). The electromagnetic field intensity inside the device can be calculated using the complex index of refraction for each material (Pettersson *et al.*, 1999).

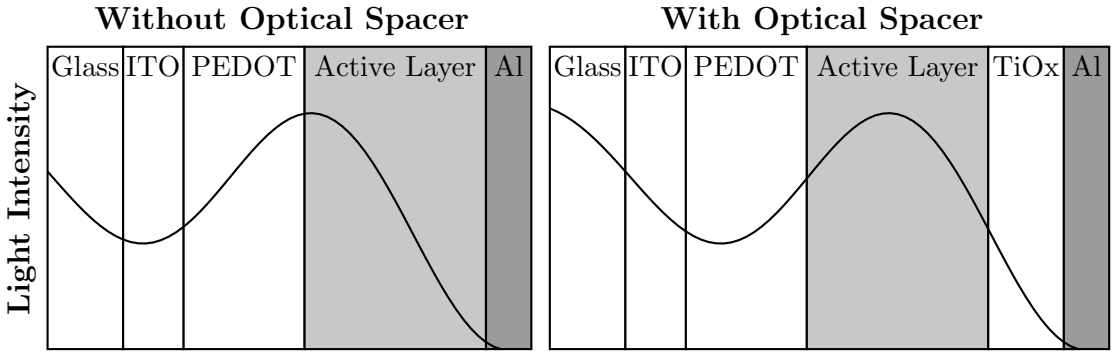

Figure 1.16: Light intensity in bulk heterojunction cells both without and with a TiO_x optical spacer (Kim *et al.*, 2006).

1.5.6 State of the Art

Tremendous progress has been made in organic photovoltaics in the last decade. Record efficiencies have more than doubled from around 5% to over 10%. Two approaches have led to these efficiency increases: the development of low bandgap polymers and the co-evaporation of polythiophene oligomers with fullerene-C_{60}.

In 2010 a group at the University of Chicago reported a 7.4% efficient organic solar cell (Liang *et al.*, 2010). They developed a series of thiophene-based polymers that absorb longer wavelengths of light and combined them with a C_{70} derivative to make up for the lower light absorption of these polymers at shorter wavelengths. Further refinement of this system by introducing additional interfacial layers has increased the efficiency to over 8% (He *et al.*, 2011) and a tandem bulk heterojunction cell using another thiophene-based low-bandgap polymer along with P3HT and two C_{60} derivatives achieved an efficiency of 10.6% (You *et al.*, 2013).

In 2012 a group at the University of Ulm in Germany reported fabrication of a 7% efficient cell that was fabricated from a polythiophene oligomer using thermal evaporation (Fitzner *et al.*, 2012). A thin film of this oligomer has an absorption spectrum that is red-shifted 72 nm relative to the absorption spectrum of the oligomer

in solution. The authors attribute this to ordered packing of oligomers in the film which is supported by a grazing-incidence X-ray diffraction (GIXRD) spectrum of the film. The width of the peak in this spectrum suggests a crystal size of about 6 nm and surprisingly this peak is not only retained but becomes narrower when the oligomer is co-evaporated with C_{60} suggesting a crystal size of 40 nm in the blended film. Subsequent work on this technology has resulted in a certified efficiency of 12% for a tandem cell which is being commercialized by Heliatek in Germany.

Activity in the field of organic photovoltaics (OPVs) is increasing quickly. In 2007 there were fewer than 100 refereed articles published on the subject. In 2013 that number increased to more than 700. Recent reports of efficiencies over 10% are lending credibility to the field and renewing interest in commercialization of OPV technologies. Nevertheless, there is a long way to go for OPV technologies to reach a maturity level which will allow them to contribute significantly to reducing the use of fossil fuels.

Chapter 2

PREPARATION AND STRUCTURAL CHARACTERIZATION

2.1 Cyclic Voltammetry

Films of two porphyrin electropolymers were formed on FTO substrates by oxidative electropolymerization of **1** and **2** in Figure 2.1. The polymers resulting from the electropolymerization of **1** and **2** are referred to as **poly1** and **poly2** respectively. Polymer films were prepared using FTO coated glass substrates measuring 1 cm by 5 cm purchased from Hartford Glass. The substrates were cleaned by sonication in a 20% v/v solution of ethanolamine in deionized water at 80 °C for 15 minutes and then rinsed with deionized water and dried in a vacuum oven. Unless otherwise stated, each substrate was then treated by placing it in a vial with 1 mL of chlorotrimethylsilane, 1 mL of N,N diisopropylethylamine, and 8 mL of freshly distilled toluene at 60 °C for 3 days. Each substrate was then removed from its vial, rinsed with dry toluene and dried in a vacuum oven.

Poly1 films were formed on these substrates via cyclic voltammetry (CV) in an acetonitrile solution containing **1** and tetra-n-butylammonium hexafluorophosphate ($TBAPF_6$). The solution was prepared by adding 7 mg of **1** to 20 mL of acetonitrile containing 0.1 M $TBAPF_6$. Each substrate was placed in a 4 cm tall square vial along with a Ag/AgCl quasi-reference electrode and a counter electrode that consisted of a coiled platinum wire enclosed in a glass tube filled with 0.1 M $TBAPF_6$ in acetonitrile and separated from the working solution by a porous glass frit. An aligator clip was connected to the portion of the substrate above the surface of the solution and the potential was scanned from 0 V to 1.5 V at 100 mV/s repeatedly until the target

optical density was achieved. After polymerization the portion of the substrate that was submerged in the solution is covered with a **poly1** film. The substrates were then rinsed with distilled acetonitrile and dried in a vacuum oven.

Figure 2.2 shows CV data from the polymerization of a **poly1** film. The broad oxidative peak between 1 V and 1.2 V is largest on the first scan and shrinks with each successive scan. It has no corresponding reductive peak which is consistent with the oxidation of **1** and formation of a new material. The oxidative peak near 0.9 V is not seen until the second scan and grows with each successive cycle as does its corresponding reductive peak near 0.8 V on the reverse scan. This is also consistent with the formation and growth of a new material on the electrode surface. The new material's lower oxidation potential suggests that it has a larger π-conjugated system than **1**.

Model compound **3**, which has a phenyl ring attached to the 15-position of the porphyrin macrocycle, does not electropolymerize when subjected to the same conditions as **1**, indicating that the 15-position on the porphyrin macrocycle is involved in the electropolymerization of **1**.

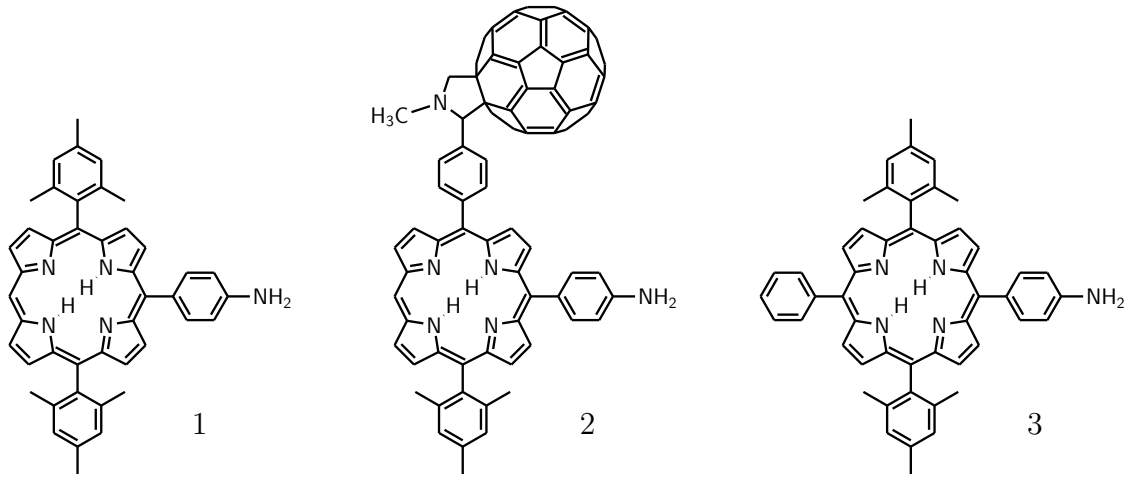

Figure 2.1: Porphyrin monomer **1**, porphyrin-fullerene monomer **2**, and porphyrin model compound **3**.

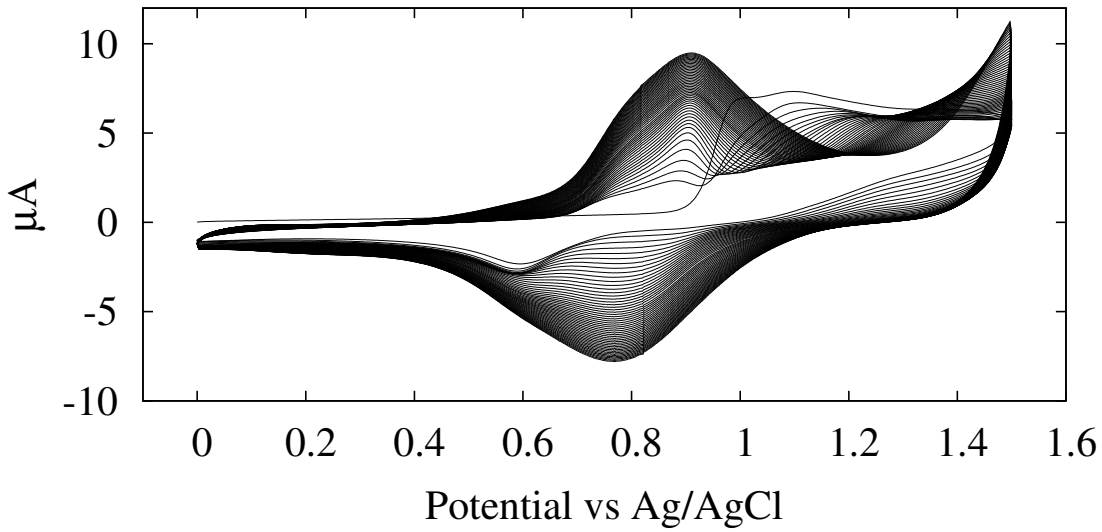

Figure 2.2: Cyclic voltammagram of **poly1** film formation.

The process used to form **poly2** films on FTO substrates was similar to that for **poly1**, but a different solvent and potential range were used. Monomer **2** is not soluble in acetonitrile so a saturated solution of **2** in dichloromethane containing 0.1 M $TBAPF_6$ was used for electropolymerization. The potential was scanned from -0.25 V to 1.3 V vs Ag/AgCl during repeated CV cycles in order to achieve the desired optical density. After polymerization the **poly2** covered substrates were rinsed with distilled dichloromethane and dried in a vacuum oven. The cyclic voltammagram of this process is shown in Figure 2.3. The CV has an oxidation peak near 0.9 V that grows with each cycle as does its corresponding reduction peak near 0.6 V.

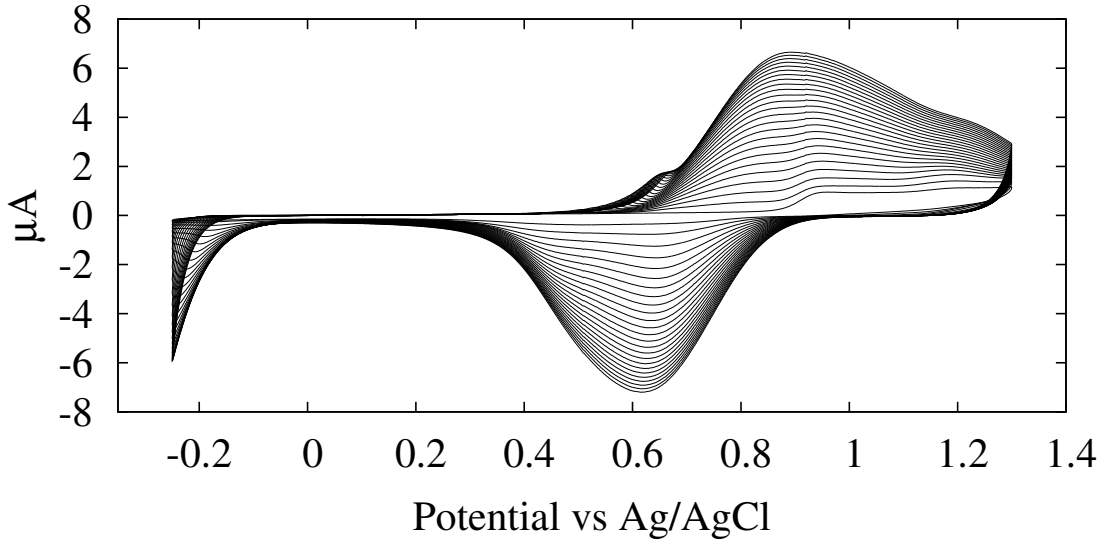

Figure 2.3: Cyclic voltammagram of **poly2** film formation.

2.2 Ultraviolet-Visible Spectroscopy

Ultraviolet-Visible absorption spectrum of polymer covered substrates were taken using a Shimadzu UV-3600 spectrophotometer. The substrates were held in place by a Shimadzu spring loaded sample holder designed to hold solid samples. All substrates were oriented with the polymer film facing the light source. Six spectra were taken on each substrate. The spectra were taken at the same spots that were contacted by mercury for electrical measurements. The spectrum of the FTO substrate was subtracted from these spectra prior to preparation of all figures and calculations.

The absorption spectra of **1** and three **poly1** films with different optical densities are shown in Figure 2.4. The absorption peak of these films are around 424 nm and are blue shifted slightly in thicker films relative to their thinner counterparts. The absorption spectra of **2** and three **poly2** films with different optical densities are shown in Figure 2.5. The absorption peaks of the **poly2** films are around 434 nm, red-shifted relative to **poly1** films. The absorption peaks in thicker **poly2** films are

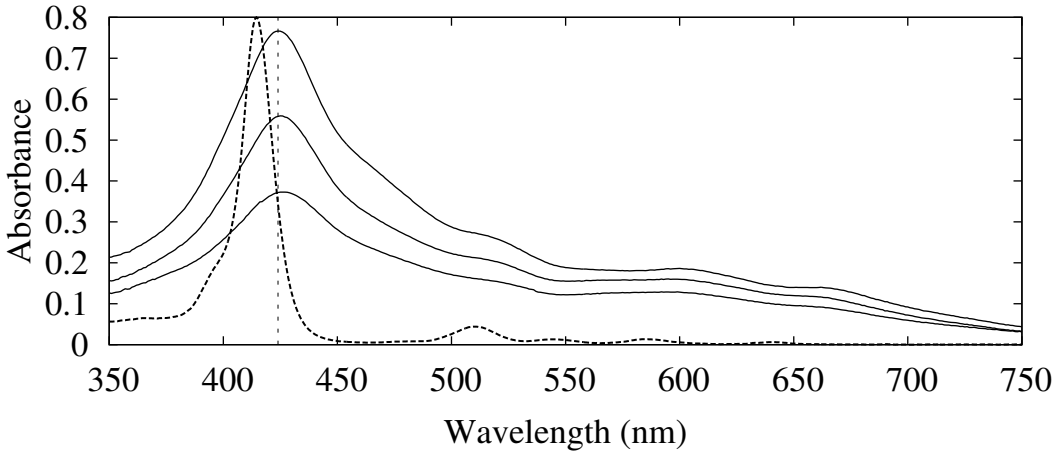

Figure 2.4: Absorption spectra of three **poly1** films (solid curves) and a normalized spectrum of **1** (thick dashed curve). The dashed vertical line at 424 nm was added as a guide to the eye.

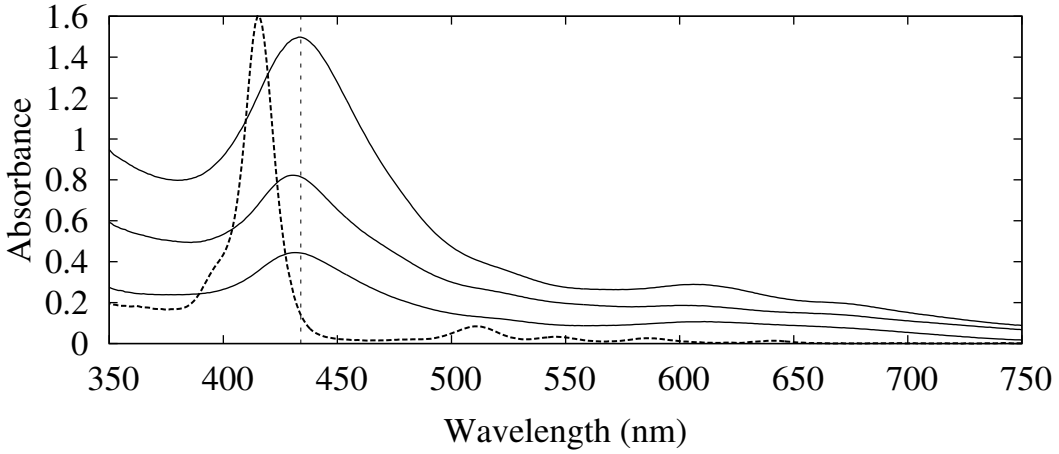

Figure 2.5: Absorption spectra of three **poly2** films (solid curves) and a normalized spectrum of **2** (thick dashed curve). The dashed vertical line at 434 nm was added as a guide to the eye.

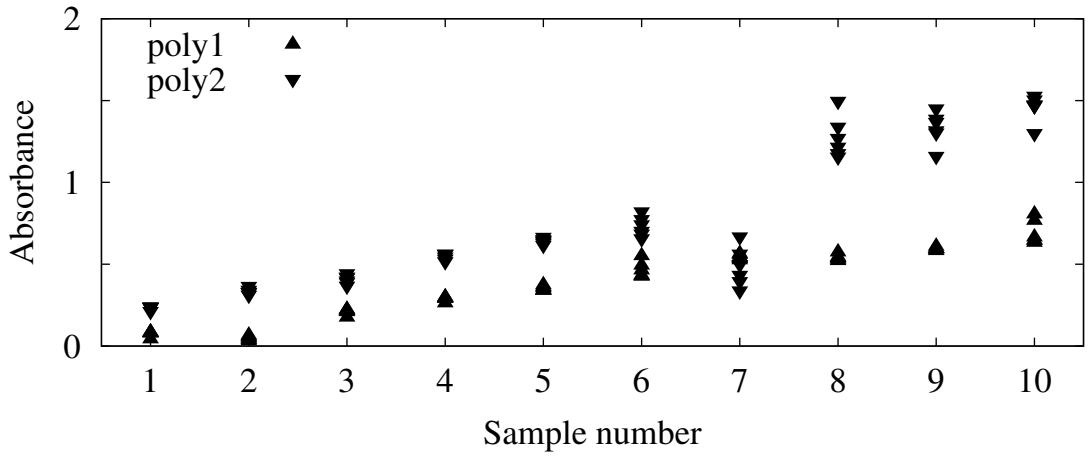

Figure 2.6: Peak absorbance from 120 spots tested on **poly1** and **poly2** samples.

red-shifted slightly relative to their thinner counterparts. Ten **poly1** films and ten **poly2** films were prepared on FTO substrates as described in Section 2.1. Figure 2.6 shows the peak absorbance between 400 and 500 nm, where the porphyrin's Soret absorption band is found, from all 120 spots tested on all 20 samples.

Profilometry and scanning electron microscopy (SEM) were used to obtain estimates of polymer film thicknesses for the purposes of correlating film thickness with optical density. For SEM imaging, polymer samples were prepared on FTO as described in Section 2.1 and their ultraviolet-visible absorption spectra were taken as described in Section 2.2. They were covered with gold by sputtering to protect the film and provide contrast for SEM images. A Nova 200 NanoLab focused ion beam system was used to cut cross sections in the samples. Platinum was deposited on top of the samples for additional protection from ion beam imaging prior to cross sectioning and images like the one in Figure 2.7 were taken of the cross sections using the Nova's built-in scanning electron microscope.

For profilometry measurements, polymer films were grown on FTO substrates and the thicknesses were determined using a Sloan Dektac II Profilometer. Linear least squares fits to correlate the film thickness data obtained from the SEM and profilom-

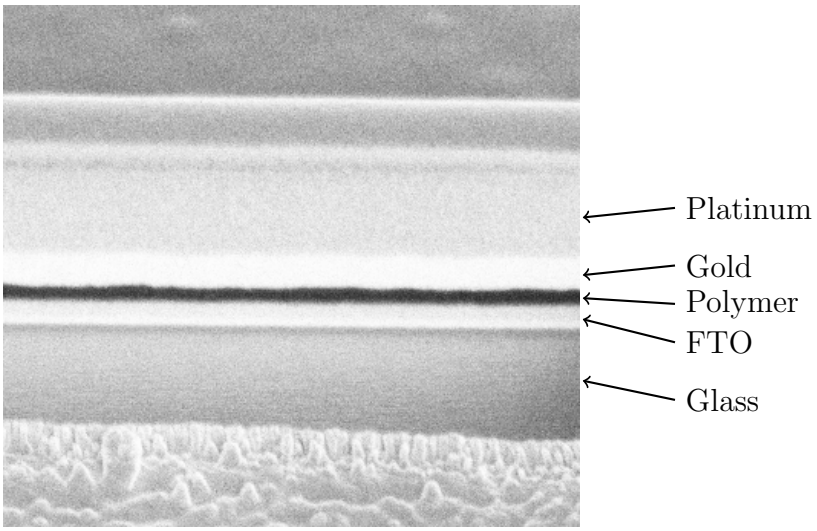

Figure 2.7: Scanning electron microscopy image of a **poly1** film cross section.

etry measurements with the optical density of the films resulted in film thicknesses of 101 nm per unit absorbance for **poly1** and 74 nm per unit absorbance for **poly2** (Gervaldo *et al.*, 2010).

2.3 Mass Spectrometry

A small amount of material was extracted from a **Poly1** film using pyridine and analyzed by matrix-assisted laser desorption/ionization-time of flight (MALDI-TOF) mass spectrometry using a terthiophene matrix. The positive ion spectrum contained peaks at m/z 637.06, 1272.10, 1907.14, 2542.16, 3177.16, 3811.16, and 4445.12 as shown in Table 2.1. Each peak is separated from the last by ~635. The exact mass of **1** is 637.32, therefore this spectrum is consistent with the polymerization of a polymer like **poly1** shown in Figure 2.8 in which two hydrogens are lost each time a monomer unit is added to the polymer chain. One hydrogen is lost from the nitrogen on the phenyl amine substituent and the other is lost from the 15-position on the porphyrin macrocycle.

Table 2.1: MALDI-TOF Peaks for material extracted from a **poly1** film.

MALDI Peaks (m/z)	Increase from Previous Peak (m/z)
637.06	-
1272.10	635.04
1907.14	635.04
2542.16	635.02
3177.16	635.00
3811.16	634.00
4445.12	633.96

Table 2.2: MALDI-TOF Peaks for material scraped from a **poly2** film.

Exact Mass for n = 1,2,3	MALDI Peaks (m/z)
1370.32	1370.06 and 1371.06
2740.62	2740.41 and 2739.41
4106.92	4106.00

A small amount of material was scraped from a **poly2** film and sonicated with a terthiophene matrix. In reflective mode, the negative ion MALDI-TOF spectrum contains peaks at m/z 1370.06, 1371.06, 2739.41, and 2740.41. In linear mode a peak was observed at m/z 4106. These results are summarized in Table 2.2 along with the exact masses for a monomer, dimer, and trimer of the **poly2** structure shown in Figure 2.8.

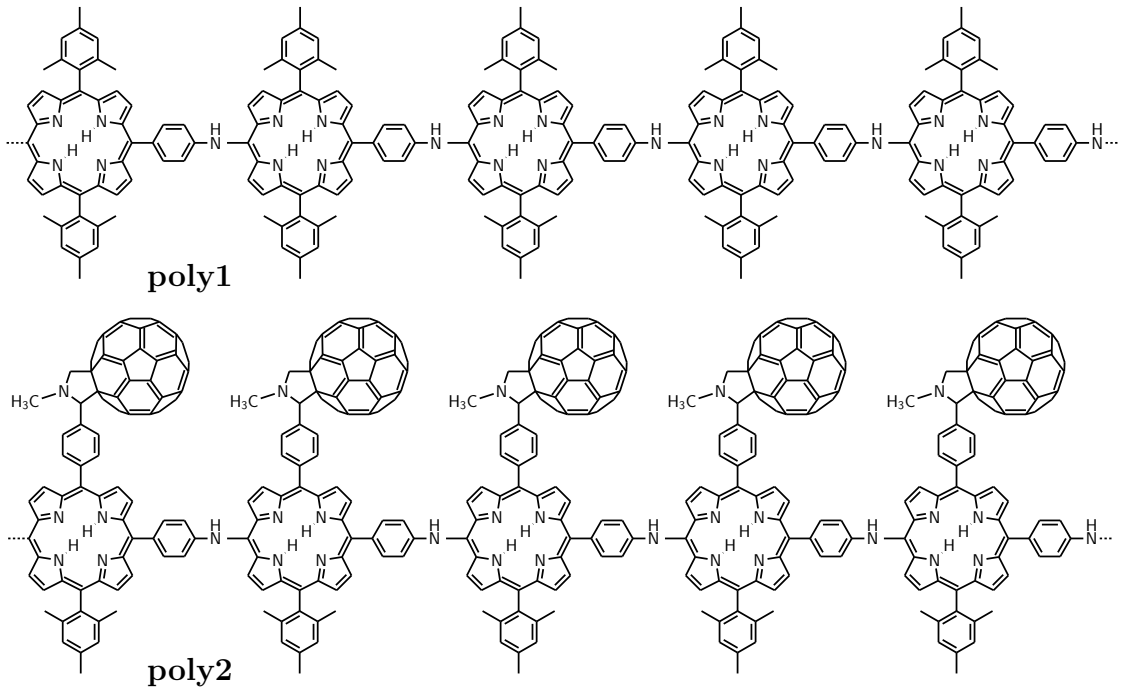

Figure 2.8: Porphyrin electropolymer, **poly1** and porphyrin-fullerene electropolymer, **poly2**.

2.4 Infrared Spectroscopy

The structure of **poly1** was investigated using Fourier transform infrared spectroscopy (FTIR). The FTIR spectra of **1**, **poly1**, and model compound **4**, which is shown in Figure 2.9, were taken using the total internal reflectance method. The spectrum of **1** was obtained by drop casting it from solution on to the surface of an attenuated total reflection (ATR) accessory in a Bruker IFS 66V/S infrared spectrometer. The ATR was in a vacuum chamber that was evacuated prior to measurement. The same process was used to obtain the spectrum of **4**. The spectrum of **poly1** was taken by using a sample holder to press a film deposited on gold covered FTO against the ATR surface.

The spectra of **1**, **4**, and **poly1** in the region between 600 cm^{-1} and 1200 cm^{-1} are shown in Figure 2.10. The spectra were normalized to have the same peak intensity

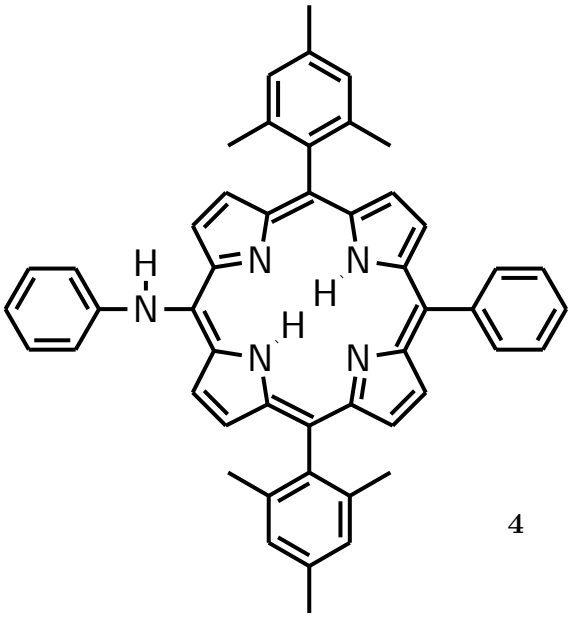

Figure 2.9: Porphyrin compound 4 was used as a model for **poly1** in IR measurements.

at 802 cm^{-1}. This peak has been assigned to the out-of-plane bending motion of the pyrrole N–H bond, and the C_β–H bond, along with a folding motion of the pyrrole ring (Zhang *et al.*, 2005; Radziszewski *et al.*, 1995). All of these bonds are the same in **1**, **4**, and the **poly1** structure shown in Figure 2.8. The peak at 850 cm^{-1} has been assigned to the out-of-plane bending motion of the C–H bond at the 15-position on the porphyrin macrocycle which is present in **1**, but not in **poly1** or **4**. The FTIR spectra confirm that this peak is larger in **1** than in **poly1** and **4** and is therefore consistent with the proposed structure of **poly1**.

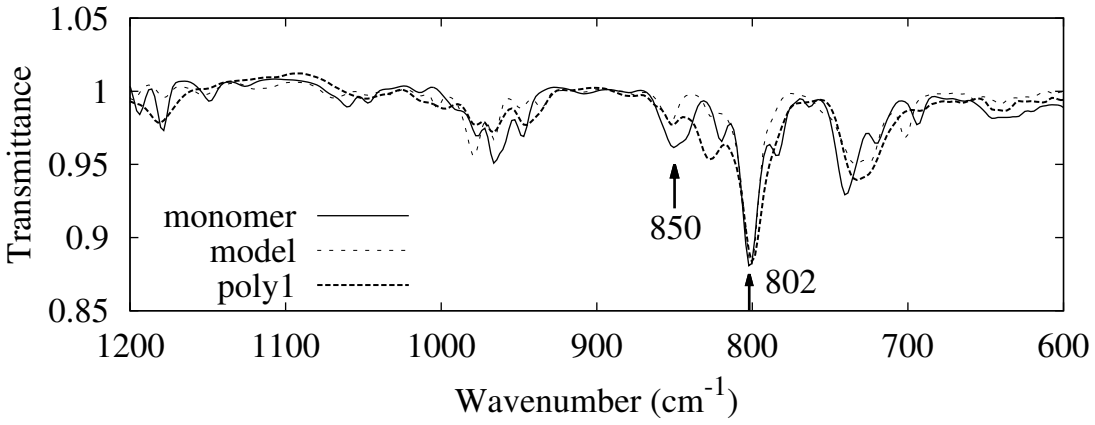

Figure 2.10: Infrared spectroscopy spectra for monomer, **1**, model compound, **4**, and **poly1** on a gold coated ITO substrate.

Chapter 3

ELECTRICAL CHARACTERIZATION

3.1 Lamp Calibration

The white light used for measuring current-voltage curves was produced by a Ushio UXL-306 xenon arc lamp powered by an Oriel 68811 power supply at 300 Watts. The light passed through a SPEX1681 monochromator with the diffraction grating set to the proper angle for white light output, then through an Oriel AM1.5 filter and a quartz lens before being directed downward by an aluminum mirror. The light then passes through a quartz window in the sample holder and onto the sample. The spectral irradiance of this white light was measured using eighteen bandpass filters. A calibrated photodiode (Newport 818-UV) measured the irradiance transmitted by each bandpass filter. The transmittance spectra of the filters are shown in Figure 3.1.

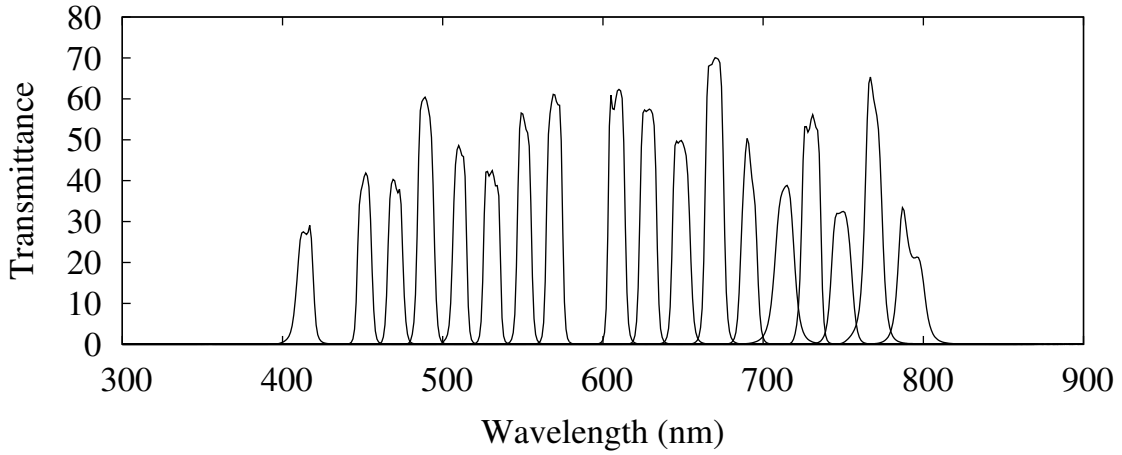

Figure 3.1: UV-Vis transmittance spectra of the bandpass filters used to characterize the white light spectral intensity.

The irradiance at the photodiode was calculated by measuring the diode's current for each filter and converting it to power using the diode responsivity at the wavelength in the center of the filter's transmission spectrum. The corresponding irradiance was calculated by dividing this power by the area of the photodiode. This irradiance, $I_{photodiode}$, corresponds to the integral in Equation 3.1 where $I_{light}(\lambda)$ is the wavelength dependent spectral irradiance of the white light and $T_{filter}(\lambda)$ is the wavelength dependent filter transmittance.

$$\int_0^\infty I_{light}(\lambda)T_{filter}(\lambda)\ d\lambda = I_{photodiode} \tag{3.1}$$

In general there is no unique solution for $I_{light}(\lambda)$, but if the white light spectral irradiance is assumed to be constant over the narrow passband of the filter then the white light spectral irradiance over this wavelength interval is given by Equation 3.2.

$$I_{light} = \frac{I_{photodiode}}{\int_0^\infty T_{filter}(\lambda)\ d\lambda} \tag{3.2}$$

Using this method the white light spectral irradiance was found for each filter and these values were plotted at the center wavelength of each filter. This process was repeated with the photodiode at six different distances from the light source and the results are shown in Figure 3.2 along with the spectral intensity of the AM1.5G spectrum.

At each distance the photodiode current was also measured under white light and the relationship between total irradiance and photodiode current was determined. Figure 3.3 shows the total irradiance of the white light as a function of the photodiode current under that white light. Prior to each set of measurements, the position of the sample holder, which contained the photodiode, was adjusted in order to obtain the photodiode current corresponding to the desired irradiance.

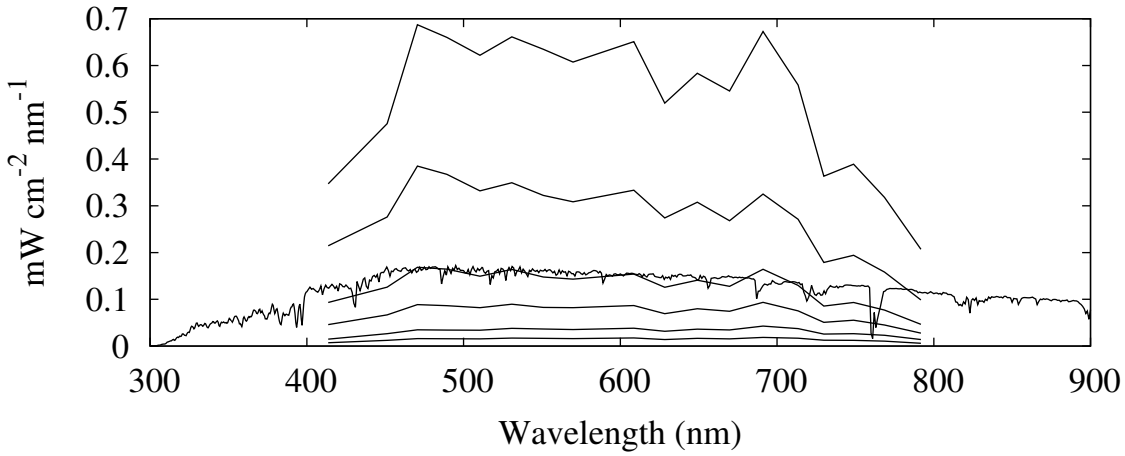

Figure 3.2: Spectral irradiance of the white light measured at six different distances from the source shown with the AM1.5G spectrum.

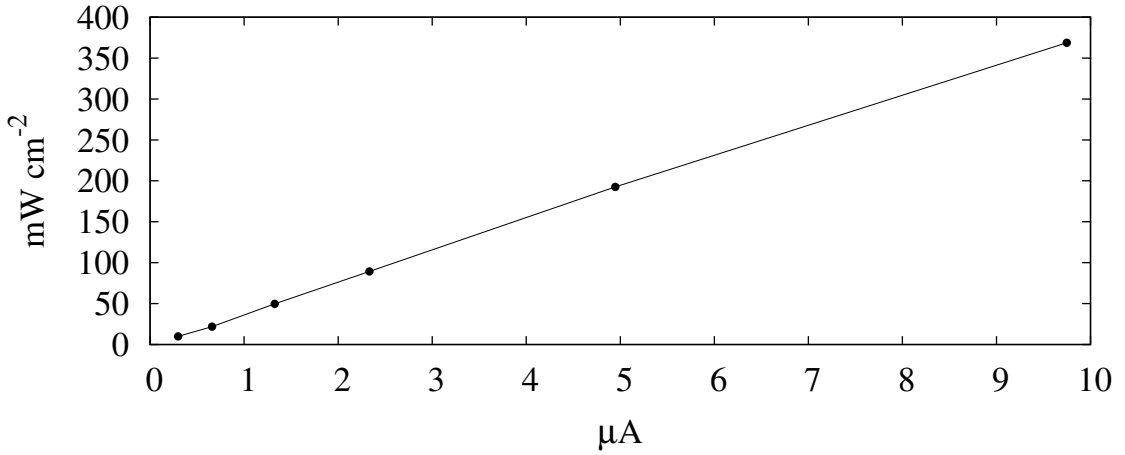

Figure 3.3: White light irradiance vs calibrated photodiode current.

3.2 Surface Treatments

3.2.1 Hexanethiol

The photovoltaic properties of these two polymers have been characterized by preparing films on FTO substrates and making electrical contact with these films using the mercury drop setup shown in Figure 3.4. Samples tested with pure mercury showed a lack of consistency with regards to the direction of photocurrent. Numerous observations of small molecules modifying the behavior of metal-semiconductor

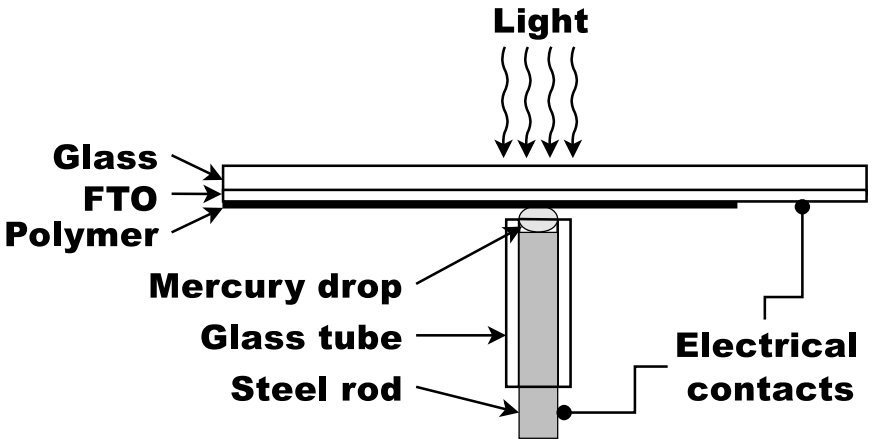

Figure 3.4: Diagram of the experimental setup used to characterize the photovoltaic properties of **poly1** and **poly2**.

interfaces have been reported (Yip *et al.*, 2008a; Liu and Yu, 2002; Zhou *et al.*, 2012; Yip *et al.*, 2008b; Ma *et al.*, 2010) so several surface treatments were tried on the mercury surface including ethanethiol, hexanethiol, decanethiol, and dodecanethiol.

Films tested using mercury treated with 10% hexanethiol in ethanol for several minutes produced unrepeatable results. Figure 3.5 shows photocurrent spectra from three spots tested on a **poly2** film contacted by mercury treated with 10% hexanethiol in ethanol. Each spot shows unique behavior with regards to the direction of photocurrent.

Treating the mercury's surface with pure hexanethiol produced the best tradeoff between photocurrent and photovoltage. Figure 3.6 shows photocurrent spectra from three spots measured on a **poly2** film using mercury treated with pure hexanethiol. The photocurrents are almost 100-fold larger than those in Figure 3.5. Treating the mercury with longer alkanethiols resulted in slightly larger photovoltages at the expense of much smaller photocurrents as shown in Figure 3.7.

The pure hexanethiol treatment consisted of putting a drop of hexanethiol in the glass tube on top of the mercury and letting it sit for 15 minutes before soaking up the excess with a tissue. The mercury surface was then allowed to dry in a nitrogen

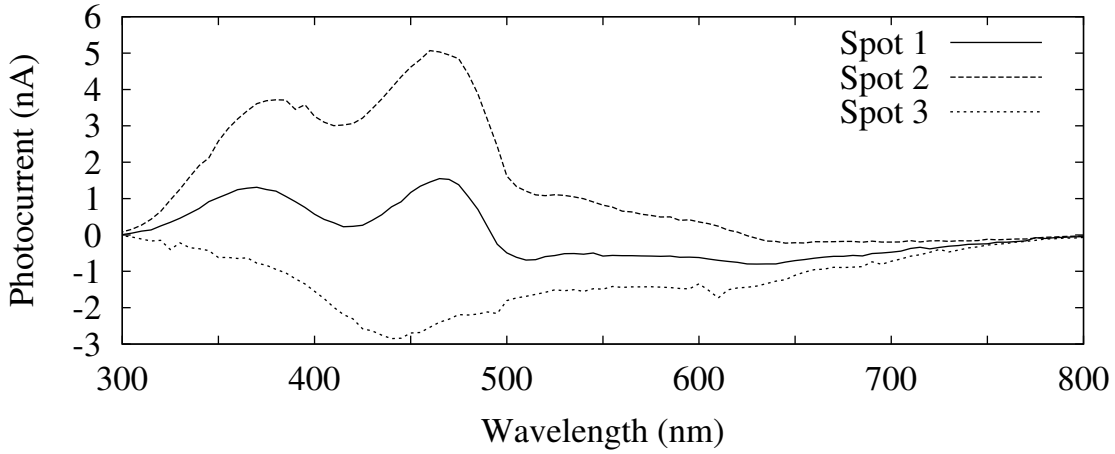

Figure 3.5: Photocurrent spectra of three spots tested on a **poly2** film. These spots were contacted by mercury treated with a 10% v/v solution of hexanethiol in ethanol.

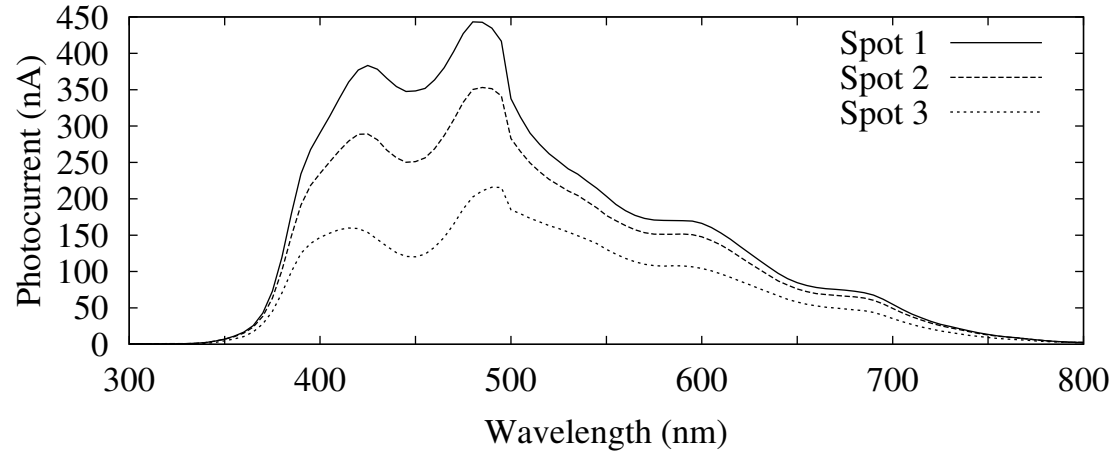

Figure 3.6: Photocurrent spectra of three spots tested on a **poly2** film. These spots were contacted by mercury treated with pure hexanethiol.

atmosphere for several minutes prior to making contact with the polymer film. Six spots were tested on each sample. Each spot was tested by bringing the mercury into contact with the polymer film until the diameter of the circular contact area was equal to the inner diameter of the glass tube holding the mercury. This resulted in a contact area of 0.086 cm^2. The distance between the spots tested was 5 mm measured from the center of one spot to the center of the next spot. An alligator clip was connected to the top of the substrate to make electrical contact with the

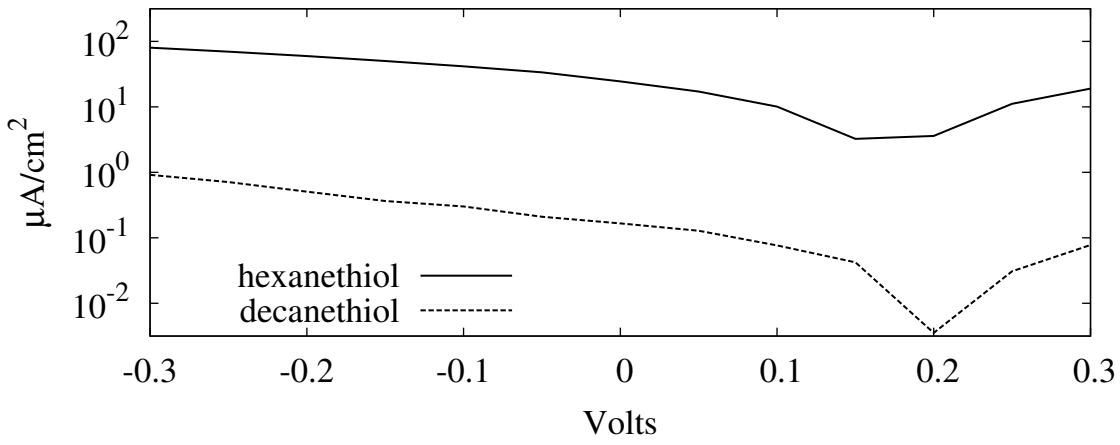

Figure 3.7: Current density-voltage curves from a **poly2** film. The solid curve was measured using mercury treated with hexanethiol. The dashed curve was measured using mercury treated with decanethiol.

FTO and another alligator clip was connected to the steel rod which supported the mercury. During all measurements the sample was under a positive pressure nitrogen atmosphere in an enclosed container.

The hexanethiol molecules on the surface of the mercury are presumed to orient themselves with the sulfur atom on the mercury surface and the hexane tail away from the surface. In this orientation the dipole moment of the hexanethiol, which is negative on the sulfur and positive on the hexane chain, creates an electric field that directs electrons away from the surface of the mercury. Surprisingly this results in photocurrent in which electrons in the polymer film are injected into the mercury and holes travel to the FTO. The reason for this becomes clear when considering the electrostatics of the system under short-circuit conditions. Figure 3.8 shows the vacuum energy levels, band energy diagrams and charge distributions of the mercury drop setup under both open-circuit and short-circuit conditions. Under open-circuit conditions there is no electric field inside the polymer and the dipole moment of the hexanethiol molecules on the mercury surface do present an energetic barrier to electrons at the polymer-mercury interface. Under short-circuit conditions the

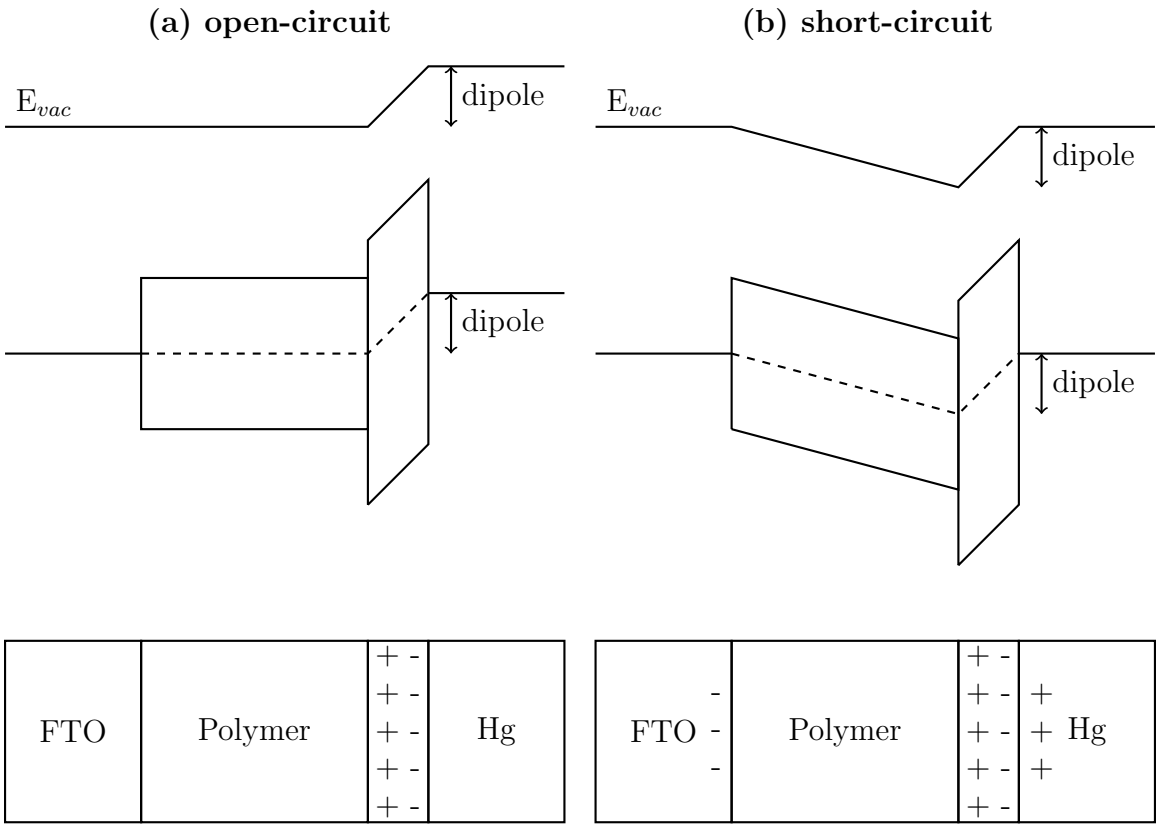

Figure 3.8: Diagram illustrating the vacuum energy levels (top), band energy diagrams (middle), and charge distributions (bottom) of the system used to characterize **poly1** and **poly2** films under open-circuit (a) and short-circuit (b) conditions.

electric field inside the polymer directs electrons to the mercury interface where they must tunnel through the hexanethiol layer. This not only explains the direction of photocurrent but also why longer alkanethiols result in lower photocurrent, but higher photovoltage. The longer alkanethiols have larger dipole moments which lead to higher photovoltages, but they present thicker tunneling barriers which result in lower photocurrents.

3.2.2 Trimethylsilane

Measurements on **Poly1** films that were electropolymerized on untreated FTO substrates produced very modest photovoltages on the order of 10 mV or less. The previously mentioned reports of small molecule modification of metal-semiconductor interfaces in addition to the maturity of silane chemistry for treating oxide surfaces resulted in a method to coat FTO substrates with trimethylsilane (TMS) groups by placing them in vials with 1 mL of chlorotrimethylsilane, 1 mL of N,N diisopropylethylamine, and 8 mL of freshly distilled toluene at 60°C for 3 days. This treatment increased the open-circuit voltage and decreased the short-circuit current density as seen in Figure 3.9 which shows current density-voltage curves from two **poly1** samples, one on a substrate treated with TMS and one on an untreated substrate. Compared to the film on the untreated substrate, the film on the substrate treated with TMS shows a decrease in short-circuit current density of 2.7 times and an increase in open-circuit voltage of 4.7 times resulting in a maximum power density that is 70% higher. The decrease in photocurrent is presumably due to the non-conductive nature of the TMS layer while the increase in photovoltage can be explained by a reduction in recombination at the FTO, polymer interface.

The discussion that follows centers around data obtained from measurements on a set of 20 polymer films. Ten of the samples consisted of **poly1** films on TMS treated FTO and the other ten were **poly2** films on TMS treated FTO. The polymer films were prepared on FTO substrates as described in Section 2.1 and the electrical properties of six spots were measured on each film.

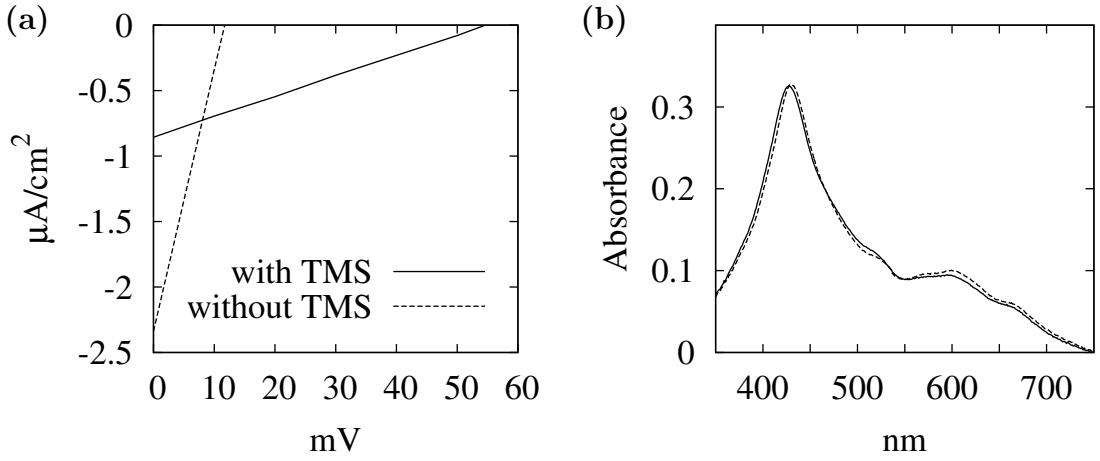

Figure 3.9: Current density-voltage curves (a) and absorption spectra (b) on two **poly1** films of nearly identical thickness. One of the two films (solid lines) was electrodeposited onto a substrate treated with trimethylsilane (TMS) and the other (dashed lines) was deposited onto an untreated substrate.

3.3 Transient Photocurrent

Transient photocurrents were measured over a period of ten seconds to ensure that the photocurrents were stable over the time scale required for spectral photocurrent measurements. The transient photocurrent measurements were performed with a Keithley 2400 source measure unit set up to record the current every second. A computer-controlled shutter determined the amount of time light was allowed to pass through to the sample. The results of these measurements on **poly1** films are shown in Figure 3.10. The shutter was closed at the beginning of each measurement. After eight seconds the shutter opened illuminating the sample and after ten more seconds the shutter closed. Figure 3.11 shows the results of transient photocurrent measurements on **poly2** films. The magnitude of these **poly2** measurements is about ten times larger than the corresponding measurements on **poly1**.

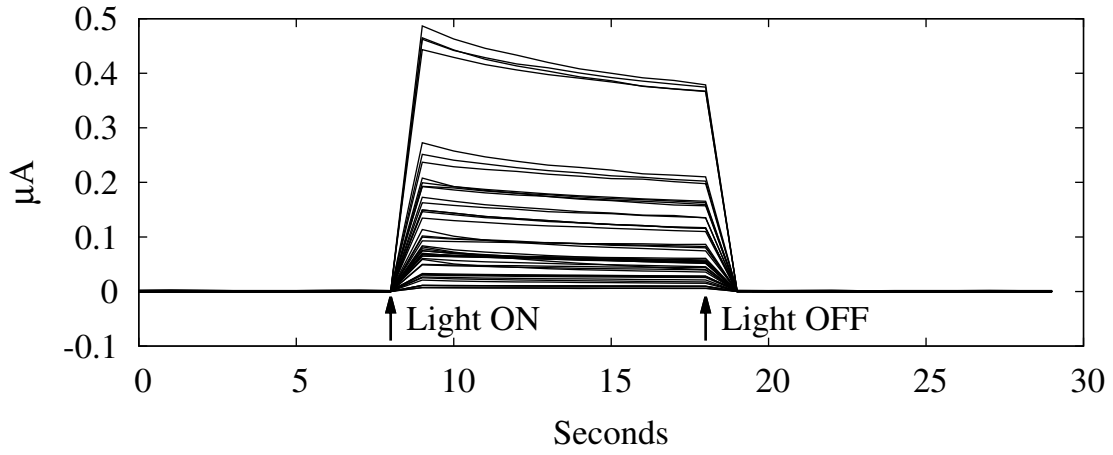

Figure 3.10: Transient photocurrent measurements from 47 spots on **poly1** films.

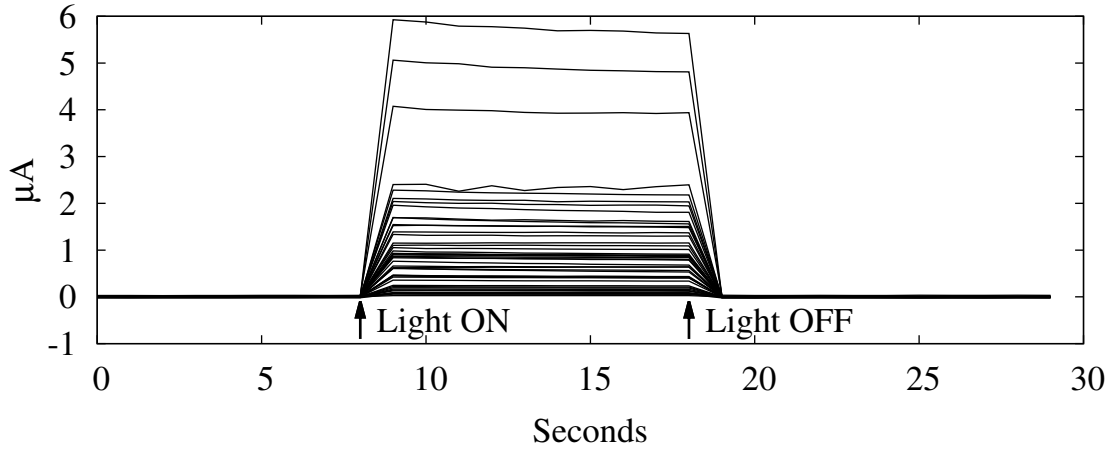

Figure 3.11: Transient photocurrent measurements from 47 spots on **poly2** films.

3.4 Incident Photon to Current Efficiency

The photocurrent spectrum of each spot was determined by measuring its short-circuit current under monochromatic light. The wavelength of the monochromatic light ranged from 800 nm down to 300 nm in 5 nm increments. At each wavelength short-circuit current was measured in the dark and then again under monochromatic light. The photocurrent at each wavelength was calculated by subtracting the current measured in the dark from the current measured under monochromatic light. A long pass filter with a cutoff wavelength near 485 nm was used to remove the monochro-

mator's short wavelength harmonics for the measurements from 800 nm to 500 nm. This filter was removed for the measurements from 495 nm to 300 nm.

Figure 3.12 shows a photocurrent spectrum from a 35 nm thick **poly1** film along with its absorption spectrum which has been corrected to remove the light absorption of the FTO substrate. The peak in the photocurrent spectrum appears to be red-shifted and dramatically broadened relative to the absorption spectrum, however this photocurrent spectrum contains features from the spectrum of the light source in addition to features from the light absorption of the **poly1** film. The calculation of IPCE normalizes the photocurrent density by the light intensity. This removes fluctuations caused by the non-uniform spectral irradiance of the light source. The IPCE spectrum of the film from Figure 3.12 was calculated from the photocurrent spectrum as described in Section 1.2.2 and the result is shown in Figure 3.13 along with the film's LHE spectrum. Comparing Figure 3.12 with Figure 3.13 demonstrates that the broadening in the photocurrent spectrum, which is not present in the IPCE spectrum, was due to the non-uniform spectral irradiance of the light source.

Although red-shifted, the IPCE spectrum in Figure 3.13 shares several features with the LHE spectrum suggesting that the photocurrent is derived from photons absorbed by the porphyrin moieties in the polymer film. The first of these shared features is the porphyrin Soret band absorption peak which is located at 428 nm in the LHE spectrum and is red-shifted to 455 nm in the IPCE spectrum. In the region between 500 nm and 700 nm, the spectra share features from the light absorption of the porphyrin Q-bands. In the LHE spectrum the first Q-band results in a slight shoulder near 510 nm. The second and third Q-bands produce a peak near 595 nm with a very slight shoulder near 575 nm and the fourth Q-band produces a shoulder near 650 nm. The IPCE spectrum has similar features that are red shifted: a shoulder near 530 nm from the first Q-band, a shoulder near 600 nm from the second and third

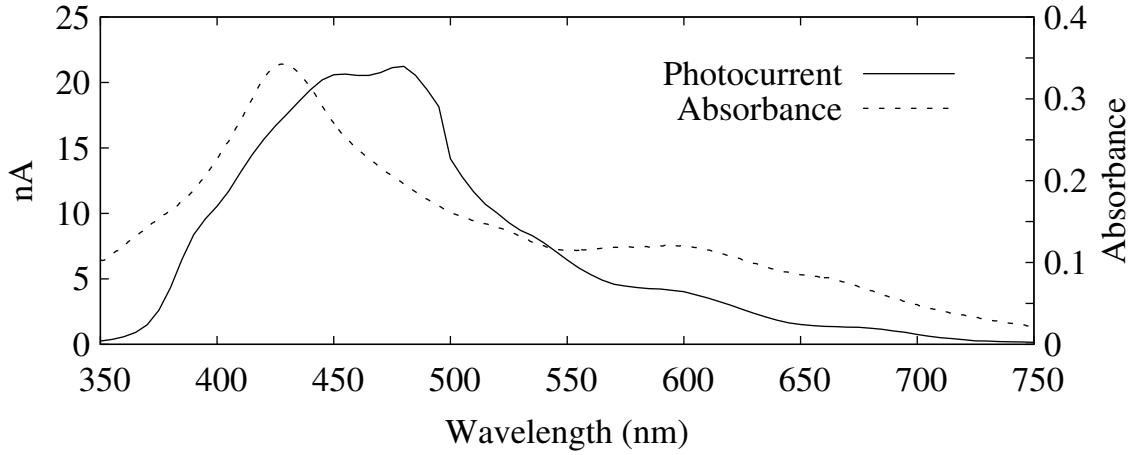

Figure 3.12: Photocurrent (solid line) and light absorption (dashed line) for a **poly1** film with a thickness of approximately 35 nm.

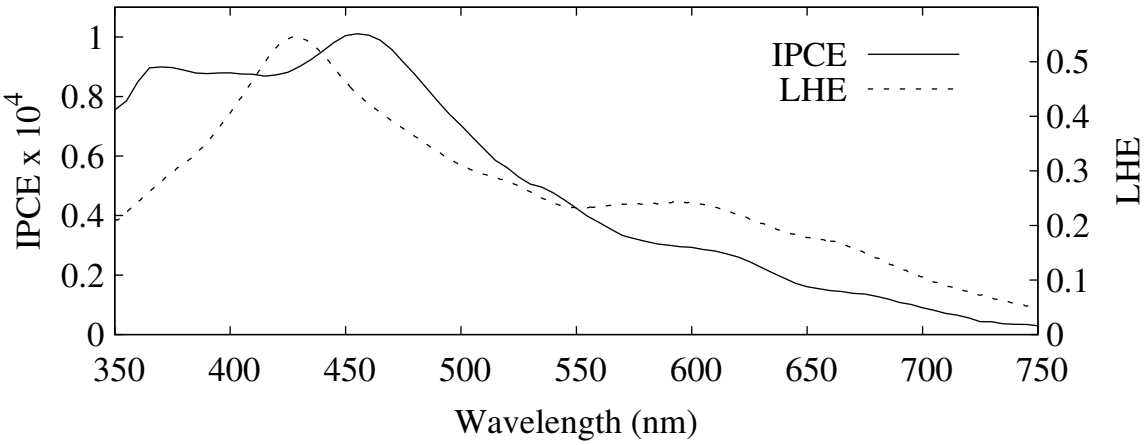

Figure 3.13: Incident photon to current efficiency (solid line) and light harvesting efficiency (dashed line) for a **poly1** film with a thickness of approximately 35 nm.

Table 3.1: Features in the absorption spectrum of compound **1** and the LHE and IPCE spectra of a 35 nm thick **poly1** film.

Compound **1** Abs	35 nm **poly1** LHE	35 nm **poly1** IPCE
414 nm	428 nm	455 nm
510 nm	510 nm	530 nm
545 nm	575 nm	600 nm
585 nm	595 nm	600 nm
641 nm	650 nm	660 nm

Q-bands, and another shoulder near 660 nm from the fourth Q-band. The appearance of three features in this region rather than the expected four for freebase porphyrins is attributed to overlap between the second and third Q-bands due to inhomogeneous broadening. The locations of these features are summarized in Table 3.1 which includes the locations of the features in the absorption spectrum of compound **1** for reference.

Figure 3.14 shows IPCE and LHE spectra from a **poly2** film with a thickness of 25 nm. These spectra also share several features which suggest that the photocurrent is derived in part from the photons absorbed by the porphyrins in this film. Fullerene light absorption may also contribute to photocurrent in **poly2** films. The features in the LHE spectrum are: a peak at 436 nm, a shoulder near 515 nm, a peak near 610 nm, and a shoulder near 660 nm. The features in the IPCE spectrum are: a peak at 455 nm, and shoulders at 525 nm, 605 nm, and 660 nm. These features are summarized along with the features from the absorption spectrum of compound **2** in Table 3.2.

In thicker **poly1** and **poly2** films IPCE decreases for high values of light harvesting efficiency where the films absorb the most light. Figure 3.15 shows IPCE and LHE spectra from a 61 nm thick **poly1** film. The IPCE spectrum in this figure contains a local minimum at 425 nm which coincides with the maximum of the LHE spectrum. Figure 3.16 shows IPCE and LHE spectra from a 111 nm thick **poly2** film. This IPCE spectrum has a local minimum at 445 nm which is red-shifted slightly from the LHE maximum at 434 nm. Both of these IPCE spectra demonstrate that, in this system, photocurrent production in thicker films of these polymers is worse at wavelengths where the most light is absorbed. This type of behavior is consistent with photocurrent generation at the cell's rear interface which can arise from the formation of a Schottky junction at this interface (Ghosh *et al.*, 1974). In this situation

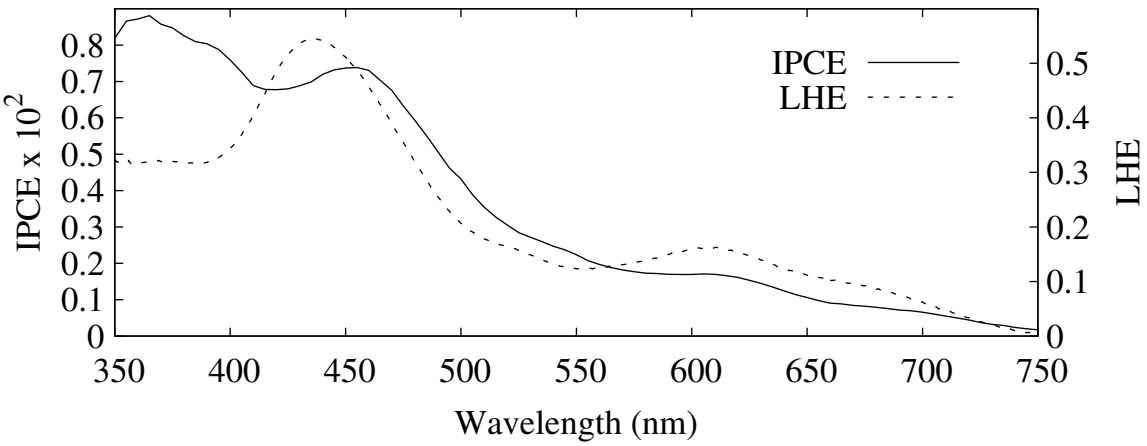

Figure 3.14: Incident photon to current efficiency (solid line) and light harvesting efficiency (dashed line) from a **poly2** film with a thickness of approximately 25 nm.

Table 3.2: Features in the absorption spectrum of compound **2** and the LHE and IPCE spectra of a 25 nm thick **poly2** film.

Compound **2** Abs	25 nm **poly2** LHE	25 nm **poly2** IPCE
415 nm	436 nm	455 nm
510 nm	515 nm	525 nm
545 nm	610 nm	605 nm
585 nm	610 nm	605 nm
640 nm	660 nm	660 nm

high LHE values, like those from the porphyrin Soret absorption band in these films, have a negative effect on IPCE because they reduce the supply of photons to the rear interface where photocurrent is produced. Thicker films essentially act as a filter, reducing the amount light that reaches the active part of the film.

The light filtering effect of these thicker films can be seen more clearly by comparing their IPCE spectra with their light transmittance spectra. The transmittance spectra provide an indication of how much light is available at the rear interfaces in these films. Figure 3.17 shows that the local minimum in the IPCE spectrum of the 61 nm thick **poly1** film coincides with the minimum in its transmission spectrum at

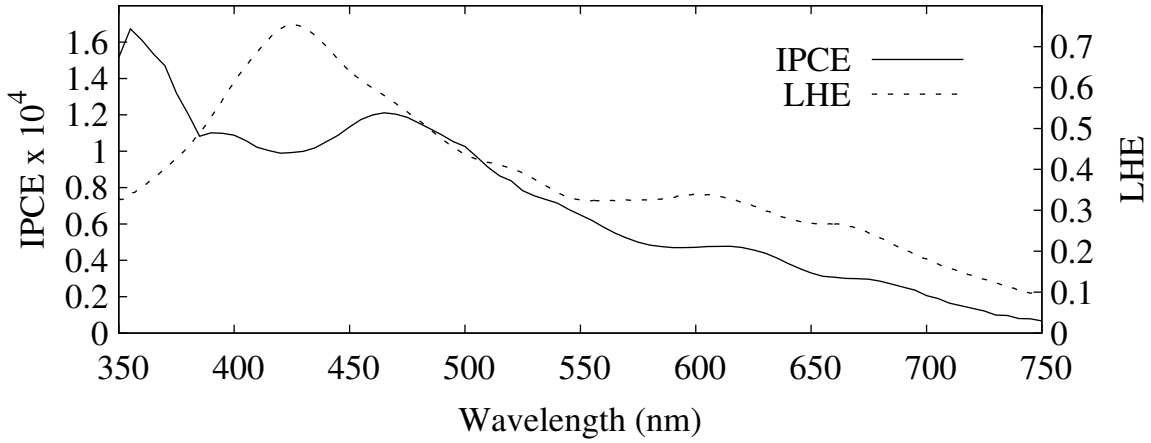

Figure 3.15: Incident photon to current efficiency (solid line) and light harvesting efficiency (dashed line) for a **poly1** film with a thickness of approximately 61 nm.

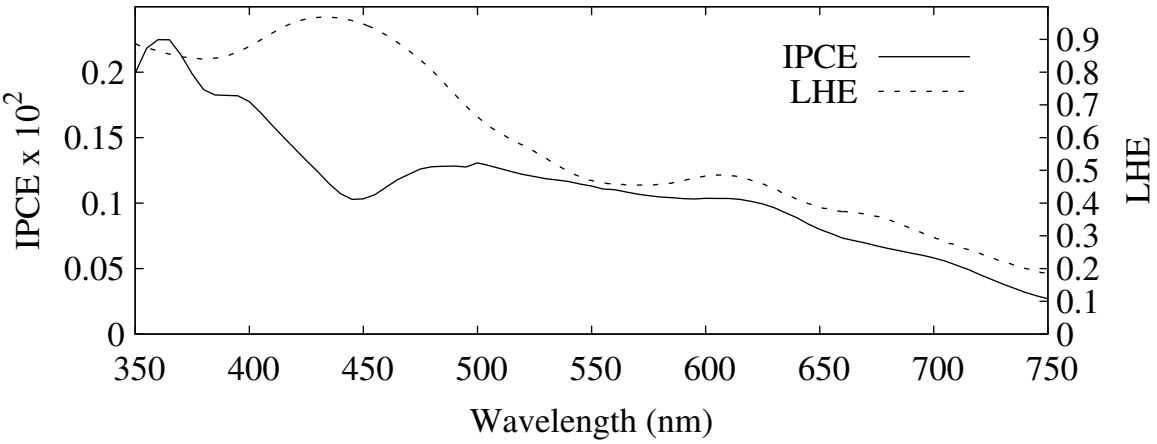

Figure 3.16: Incident photon to current efficiency (solid line) and light harvesting efficiency (dashed line) from a **poly2** film with a thickness of approximately 111 nm.

425 nm. At this wavelength only 25% of the incident light is available at the rear interface. The local minimum in the IPCE spectrum of the 111 nm thick **poly2** film is located at 445 nm, red-shifted slightly from the minimum in the transmittance spectrum at 434 nm as shown in Figure 3.18. At 434 nm less than 5% of the incident light is available at the rear interface of this film.

The red-shift between IPCE and transmittance minima in **poly2** films may be due to the presence of fullerene-C_{60} in these films. If photons absorbed by fullerenes

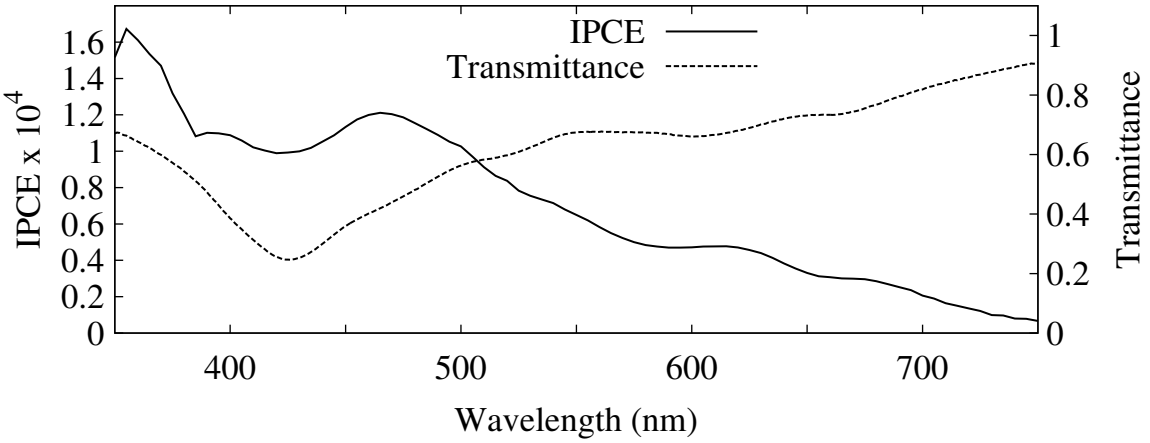

Figure 3.17: Incident photon to current efficiency (solid line) and light transmittance (dashed line) for a **poly1** film with a thickness of approximately 61 nm.

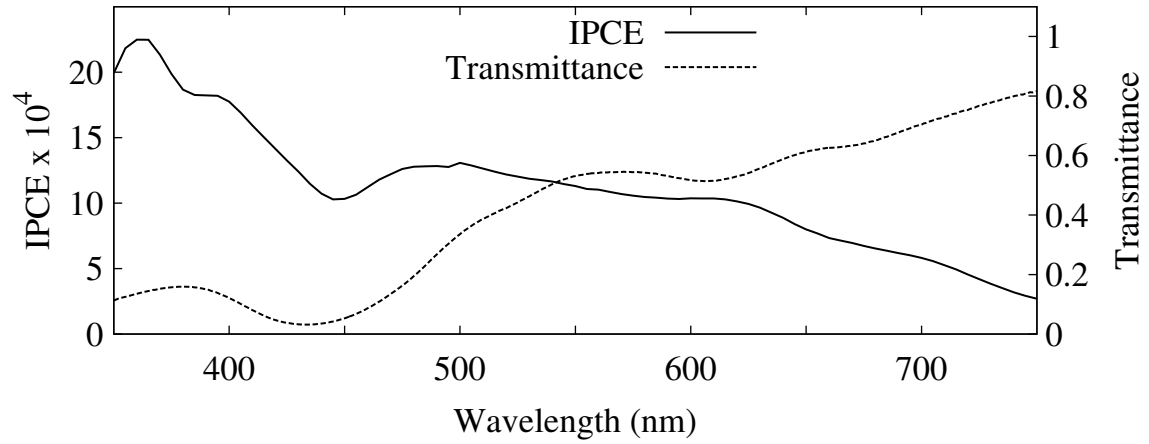

Figure 3.18: Incident photon to current efficiency (solid line) and light transmittance (dashed line) from a **poly2** film with a thickness of approximately 111 nm.

in these films are more likely to contribute to photocurrent than photons absorbed by porphyrins then the IPCE will be greater at shorter wavelengths where the fullerenes absorb light and the minima in the IPCE spectra will be red-shifted. Exciton diffusion lengths exceeding 30 nm have been reported for fullerene-C_{60} (Qin *et al.*, 2011) which may explain why photons absorbed by fullerene are more likely to contribute to photocurrent.

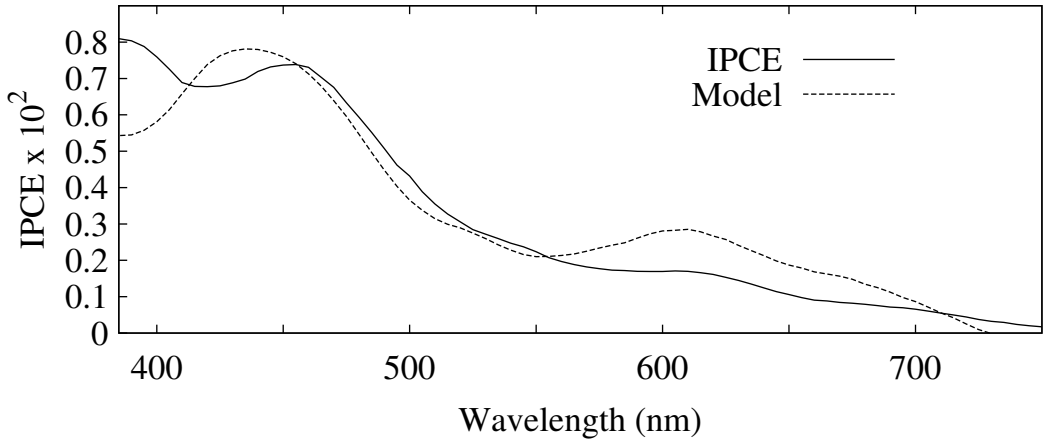

Figure 3.19: Incident photon to current efficiency (solid line) and a theoretical model for IPCE (dashed line) for a **poly2** film with a thickness of approximately 25 nm.

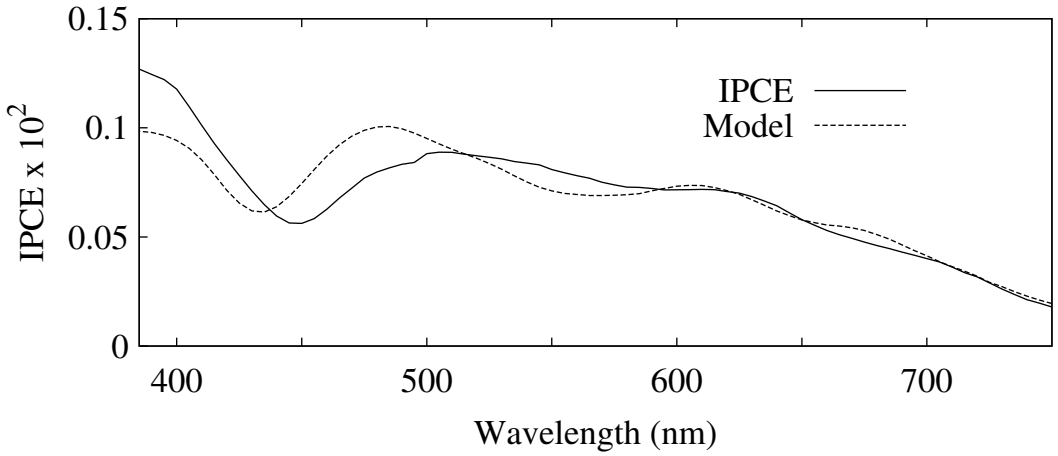

Figure 3.20: Incident photon to current efficiency (solid line) and a theoretical model for IPCE (dashed line) from a **poly2** film with a thickness of approximately 111 nm.

A theoretical model was constructed to test the hypothesis of photocurrent generation at the rear interface in this system. This model uses the absorption spectrum and thickness of the film to calculate the absorption coefficient at each wavelength in the IPCE spectrum. Using these absorption coefficients, it computes the number of photons absorbed within a small distance of the polymer-mercury interface at each wavelength. Three parameters were used to fit this model to experimental data: the distance from the mercury interface, a scaling factor, and an offset. The IPCE es-

timates from this model for the 25 nm and 111 nm thick **poly2** films are shown in Figure 3.19 and Figure 3.20. The R^2 values for these estimates are 0.91 and 0.87 respectively. This model fits surprisingly well given that it does not take into account reflection of light from the mercury surface and the resulting interference between the incident and reflected light. Modeling this optical interference requires measurement of the complex, wavelength dependent indices of refraction for each of the materials in the system (Moul and Meerholz, 2007).

IPCE indicates what fraction of photons incident upon the solar cell produce a photoexcited electron that contributes to photocurrent. The IPCE spectrum in Figure 3.13 indicates that about 1 in 10,000 photons produced an electron that contributed to photocurrent in this **poly1** film. The IPCE of the **poly2** film in Figure 3.14 was more than 70-fold better despite having a nearly identical light harvesting efficiency. These IPCE spectra demonstrate that the presence of the fullerene in **poly2** films demonstrably enhances charge separation relative to **poly1** films.

3.5 Current-Voltage Curves

Current-voltage characteristics were measured on each spot using a Keithley 2400 source measure unit. The voltage was scanned from 0 V to 0.5 V and then to -0.5 V and then back to 0 V in 10 mV increments. The current was sampled for 100 ms at each voltage. I-V curves were measured in the dark and under white light of five different intensities: 12.5 mW/cm^2, 25 mW/cm^2, 50 mW/cm^2, 100 mW/cm^2, and 200 mW/cm^2.

Figure 3.21 shows a current density-voltage curve from a **poly1** film measured under white light with an intensity of 100 mW/cm^2. The short-circuit current density, open-circuit voltage, fill factor, and maximum power density can all be found from this measurement. In this figure the short-circuit current density is 3.67 μA/cm^2, the

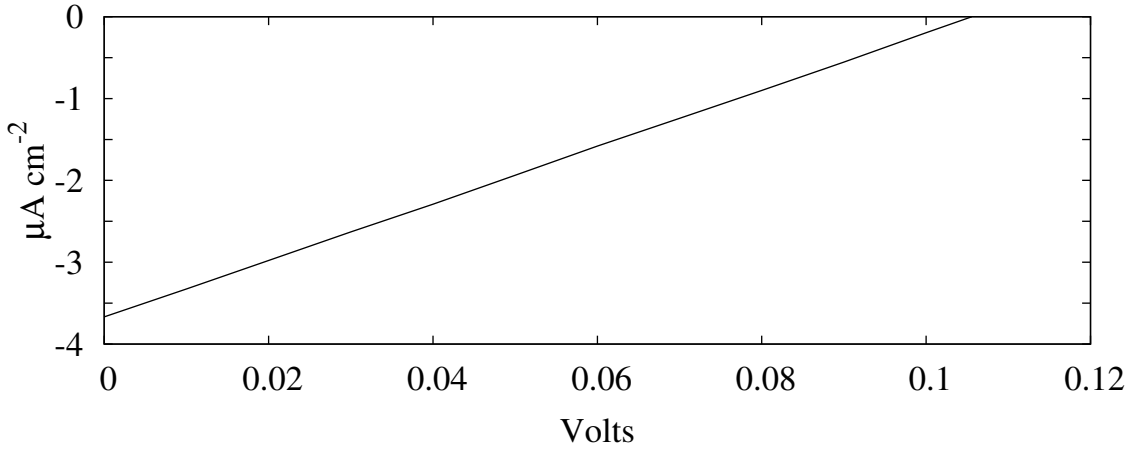

Figure 3.21: Current density-voltage curve from a **poly1** film under 100 mW/cm^2 white light.

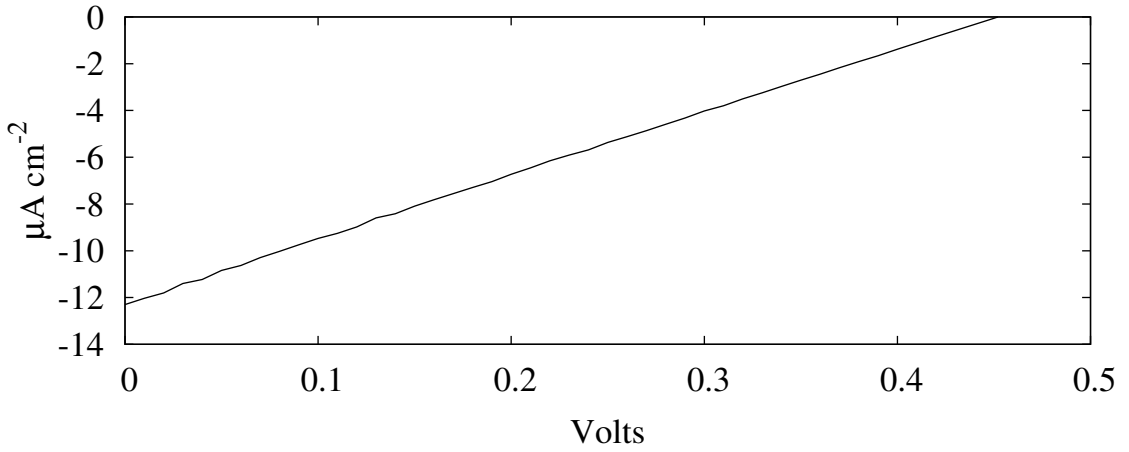

Figure 3.22: Current density-voltage curve from a **poly2** film under 100 mW/cm^2 white light.

open-circuit voltage is 0.105 V, the fill-factor is 0.25, and the maximum power density is 0.9 μW/cm^2. This power density corresponds to a power conversion efficiency of 0.0009%. Figure 3.22 shows a current density-voltage curve from a **poly2** film under 100 mW/cm^2 intensity light. The short-circuit current density is 12.3 μA/cm^2, the open-circuit voltage is 0.45 V, the fill-factor is 0.25, and the maximum power density is 7.5 μW/cm^2 which corresponds to a power conversion efficiency of 0.0075%. These linear current density-voltage curves suggest that transport losses in this system must be reduced in order to achieve high efficiency.

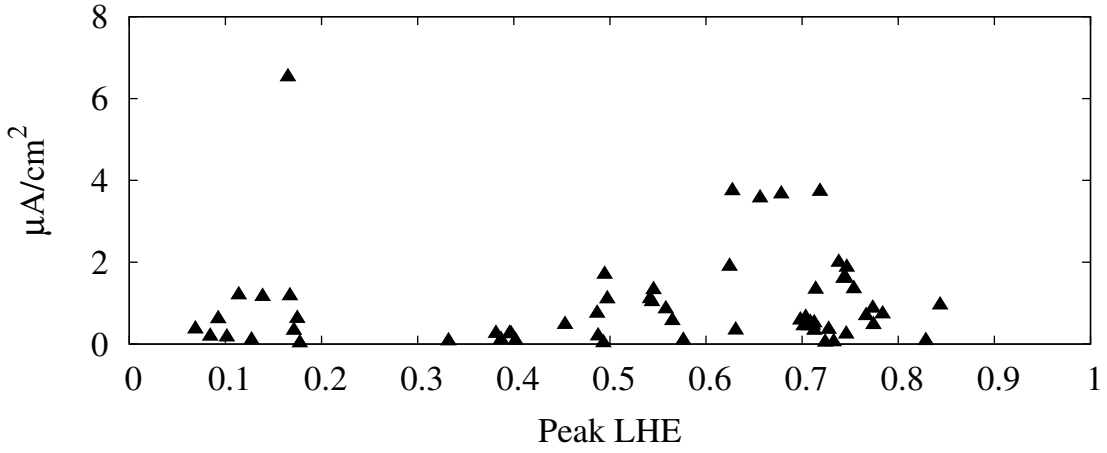

Figure 3.23: Short-circuit current density from 60 spots tested on **poly1** films under simulated AM1.5G light with an intensity of 100 mW/cm^2.

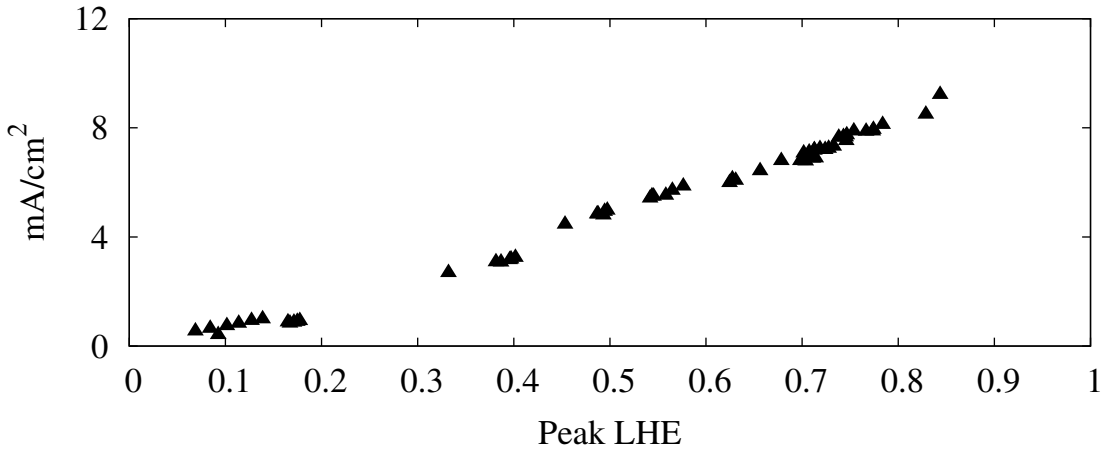

Figure 3.24: Maximum short-circuit current density possible for all spots tested on **poly1** films calculated using the LHE spectrum of each spot and the photon flux density of the AM1.5G spectrum.

3.5.1 Short-Circuit Current Density

Short-circut currents were found from current-voltage curves measured under white light with an intensity of 100 mW/cm^2. Current density was calculated from current measurements by dividing them by the area of the mercury contact, 0.086 cm^2. Figure 3.23 contains the short-circuit current densities from all 60 spots tested

on **poly1** films. These short-circuit current densities have a mean of 1.0 μA/cm^2 and a maximum of 6.5 μA/cm^2.

The fluorescence emission from **poly1** films peaks at 690 nm which corresponds to an energy gap of 1.8 eV. The maximum short-circuit current density for a solar cell utilizing a light absorber with an energy gap of 1.8 eV is 19.7 mA/cm^2 which was calculated as described in Section 1.3.1. The maximum short-circuit photocurrent density measured on **poly1** films represents about 0.03% of the maximum possible. However, this maximum was calculated assuming complete absorption of all photons with an energy greater than or equal to 1.8 eV which is not the case for these **poly1** thin films. The light harvesting efficiency spectrum of each spot tested was used to calculate its respective maximum short-circuit photocurrent density under 100 mW/cm^2 AM1.5G light using Equation 3.3 and the results are shown in Figure 3.24.

$$J_{max} = q \int_{300}^{690} LHE(\lambda)\phi_{AM1.5G}(\lambda)d\lambda \tag{3.3}$$

When compared with these revised maximum photocurrent densities, the measured values are still less than 1% of their maximums indicating that the rate of non-radiative recombination in this system is much higher than the rate of exciton dissociation. These low photocurrent yields are typical of cells which use a single organic semiconductor. They are also consistent with the viewpoint that light absorption in **poly1** films produces Frenkel excitions that have high binding energies and exciton diffusion lengths that are only long enough for a small fraction of excitons to reach the rear interface where exciton dissociation takes place.

The short-circuit current density from all sixty measurements on **poly2** films are plotted vs their peak Soret absorbance in Figure 3.25. The mean value of these measurements is 12.7 μA/cm^2 and the maximum is 65.8 μA/cm^2. This mean current density represents a greater than thirteen-fold increase compared to the mean short-

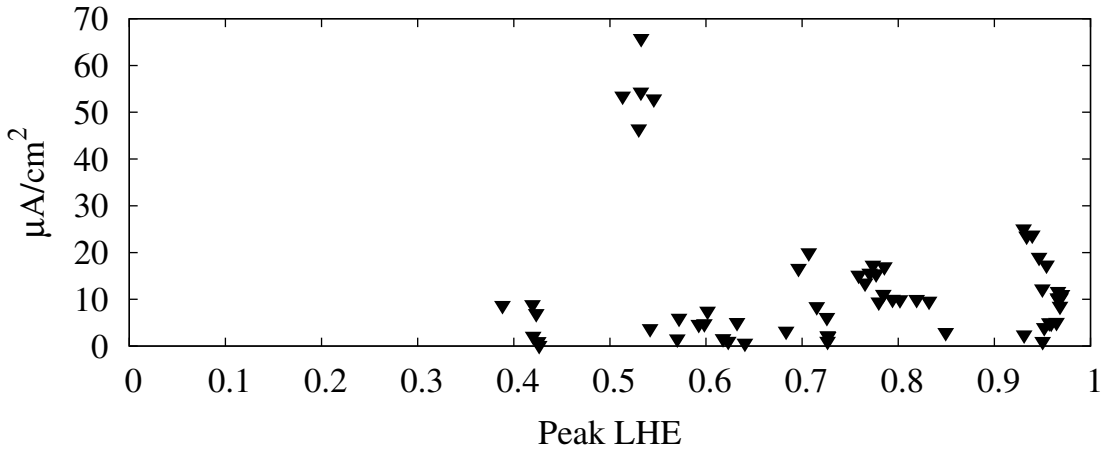

Figure 3.25: Short-circuit current density for all spots tested on **poly2** films.

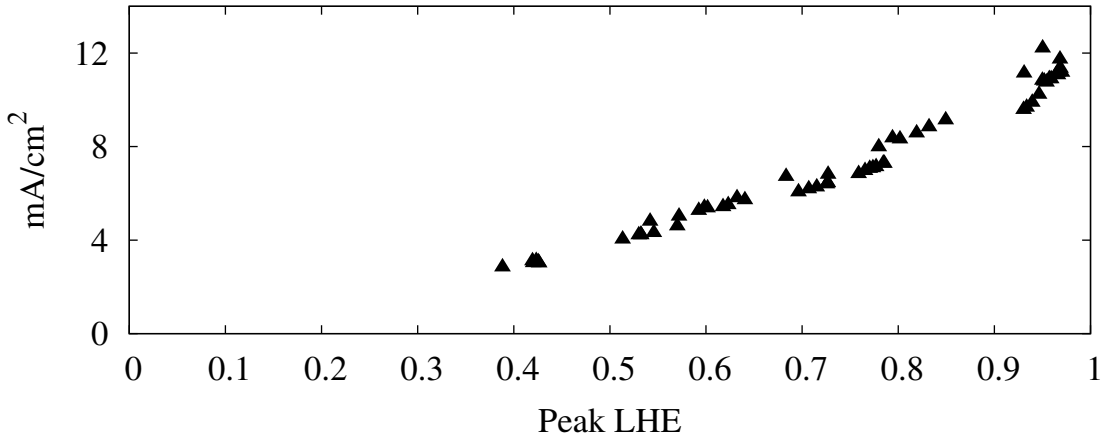

Figure 3.26: Maximum short-circuit current density possible for all spots tested on **poly2** films calculated using the LHE spectrum of each spot and the photon flux density of the AM1.5G spectrum.

circuit current density measured on **poly1** films, suggesting that the dissociation of photogenerated excitons in **poly2** films is greatly enhanced relative to **poly1** films. Nevertheless these current densities are a small fraction of the current that these films could generate based on the number of photons they absorb. The maximum possible short-circuit photocurrent density was calculated for each spot using the method described for **poly1**. The results of these calculations are shown in Figure 3.26. This method produces maximum photocurrent densities in the mA/cm^2 range for even the thinnest **poly2** films.

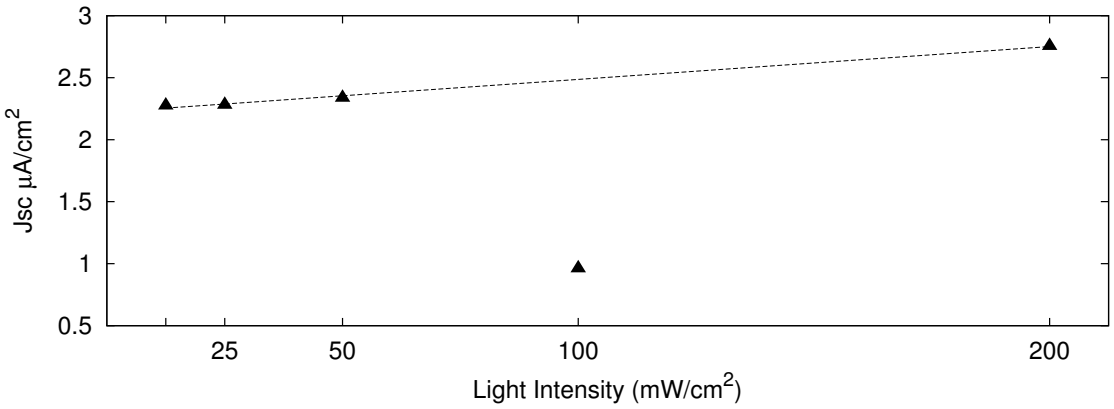

Figure 3.27: Average of sixty short-circuit current density measurements on **poly1** films at five light intensities.

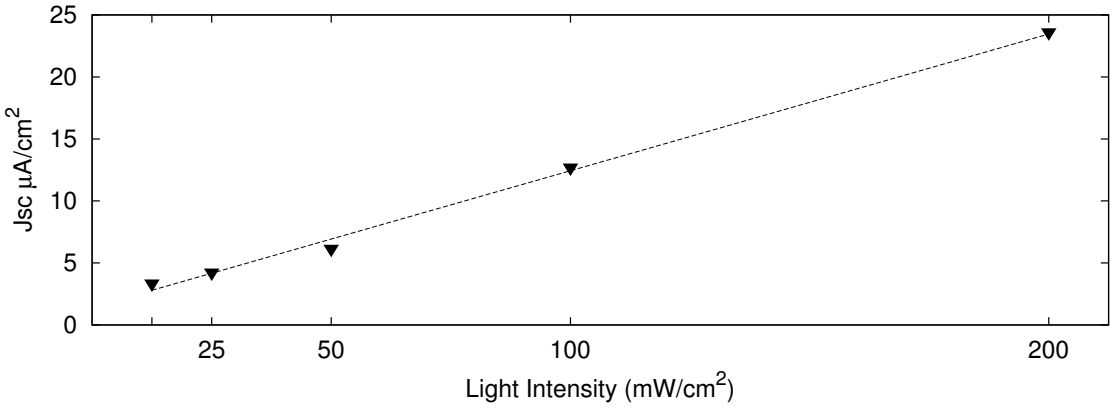

Figure 3.28: Average of sixty short-circuit current density measurements on **poly2** films at five light intensities.

The affect of light intensity on short-circuit current density was investigated by measuring I-V curves at five different light intensites. Figure 3.27 shows the results of these measurements on **poly1** films. The measurements from all sixty spots were averaged to produce each data point in the figure. Four of the five data points suggest a linear relationship between light intensity and short-circuit current density. The data point at 100 mW/cm^2 is from the first I-V curve measurement on each spot. The process of measuring an I-V curve applies a voltage across the film and was observed to change the initial performance of the device. From these measurements, it appears that the greatest change in performance occurs during the first I-V curve

measurement. These results show that increasing the light intensity 8-fold, from 12.5 mW/cm^2 to 200 mW/cm^2, produced only a 25% increase in short-circuit current density. Figure 3.28 shows the corresponding results on **poly2** films and for these films the short-circuit current density increases in proportion to the light intensity. Doubling the light intensity from 50 mW/cm^2 to 100 mW/cm^2 doubles the short-circuit current density from 6 μA/cm^2 to 12 μA/cm^2 and doubling the light intensity again to 200 mW/cm^2 doubles the current to 24 μA/cm^2. This indicates that charge separation is much more efficient in **poly2** films. Light absorption in **poly2** films produces a charge-separated state on a picosecond time scale (Gervaldo *et al.*, 2010) so the low IPCE in **poly2** films is due to either poor dissociation of this charge separated state into free electron-hole pairs or due to light absorption that is much lower than the absorption measurements on these films suggest. The reflection of light at the mercury interface could produce much lower light absorption than suggested by absorption measurements on these films.

3.5.2 Open-Circuit Voltage

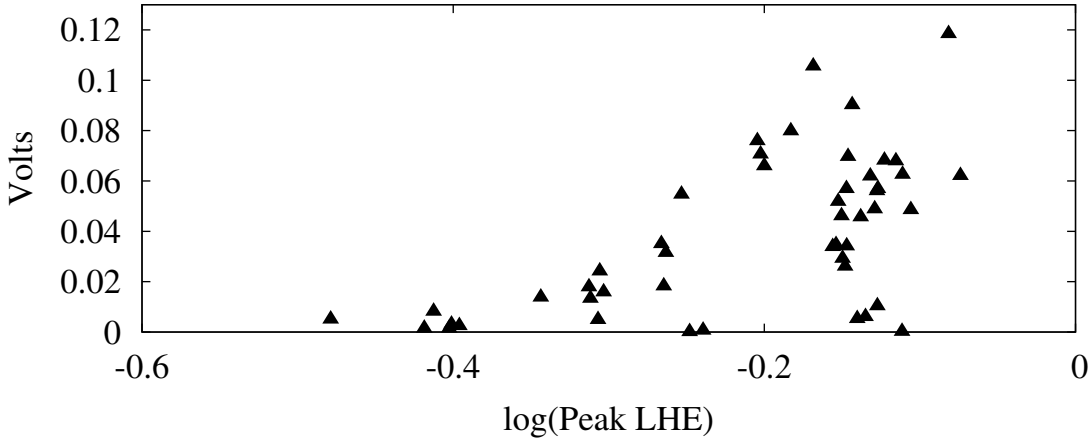

Figure 3.29: Open-circuit voltage from 60 spots tested on **poly1** films under approximated AM1.5G light with an intensity of 100 mW/cm^2.

The open-circuit voltages from sixty spots on ten **poly1** films are plotted in Figure 3.29. The mean of these measurements is 0.031 Volts and the maximum is 0.118 Volts. The open-circuit voltage of single layer organic photovoltaics is limited by the difference between the work functions of the electrodes as described in Section 1.5.1. Measured values of the work function of a material are highly dependent on the condition of the surface. Factors including crystal orientation and surface contamination affect measurements such that reported values for the work function of FTO vary from 4.4 eV to 5.0 eV (Helander *et al.*, 2011). Numerous sources report the work function of mercury to be 4.5 eV so the difference between the work functions of FTO and Mercury is somewhere between 0 and 0.5 V. In this system the effective work function of mercury is lowered by the hexanethiol on the mercury's surface. The energy diagram of this **poly1** system is shown in Figure 3.30(a). The energy of the highest occupied molecular orbital (HOMO) of **poly1** was estimated from its first oxidation potential assuming that the standard calomel electrode (SCE) is located 4.35 eV below vacuum. The energy of **poly1's** lowest unoccupied molecular orbital (LUMO) was estimated by adding the 1.8 eV estimate of the energy gap for optical absorption to the HOMO energy.

The effect of the hexanethiol layer was estimated from the dipole moment of hexanethiol and the packing density of molecules in a hexanethiol self-assembled monolayer. The potential across a layer of polar molecules is given by Equation 3.4 where p is the dipole moment of the molecules, ϵ is the permittivity, and A is the area per molecule.

$$V = \frac{p}{\epsilon A} \tag{3.4}$$

Using a dipole moment of 1.36 Debye for hexanethiol (Mathias and Filho, 1958), a dielectric constant of 4, and an area of 20 square Angstroms per molecule (Hinterwirth *et al.*, 2013) gives a voltage of 0.6 V. Using smaller areas per molecule gives

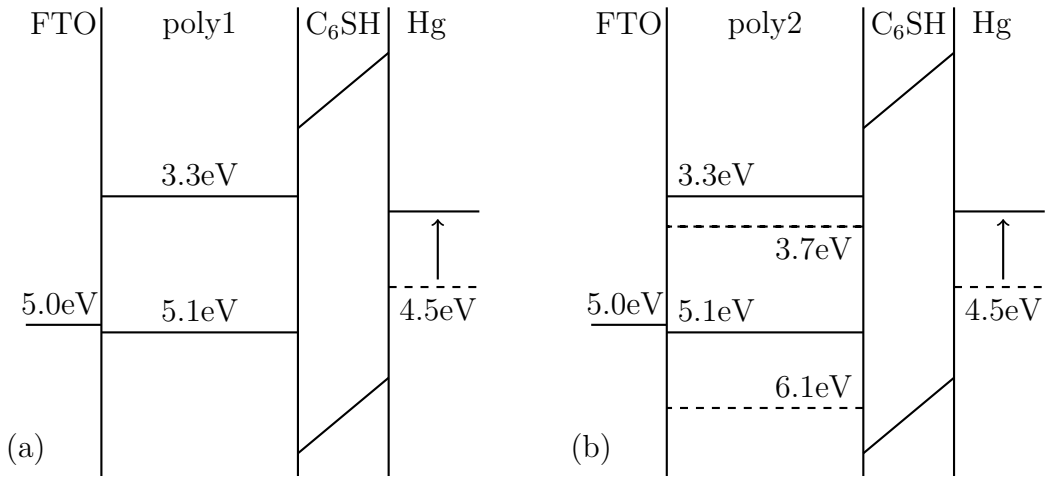

Figure 3.30: Energy level diagrams of a **poly1** film (a) and a **poly2** film (b) on FTO contacted by mercury treated with hexanethiol.

higher voltages. With hexanethiol, the effective difference between the work functions of the electrodes in this system could be 1.1 eV. The large discrepancy between the measured open-circuit photovoltages and the effective work function difference suggests that recombination in this system is much faster than charge separation. The trimethylsilane treatment of FTO was shown in Section 3.2.2 to increase the open-circuit voltage on **poly1** films which suggests that at least prior to this treatment the dominant recombination process was located at the FTO-polymer interface.

Figure 3.31 shows the open-circuit voltages of the spots tested on **poly2** films. The mean of these measurements is 0.220 Volts and the maximum is 0.452 Volts. This mean value is more than seven times larger than the mean open-circuit photovoltage measured on **poly1** samples. In order to calculate theoretical maximum photovoltages, a **poly2** bandgap of 1.8 eV was used for the purposes of light absorption. To estimate radiative losses, a bandgap of 1.38 eV was used because the quenching of fluorescence emmission in **poly2** suggests that formation of the charge separated state consisting of a porphyrin radical cation and fullerene radical anion, $P^{\bullet+}$-$C_{60}^{\bullet-}$, is much faster than emission. The theoretical maximum photovoltage will

be achieved when the only recombination losses are a result of radtiative emission from this charge separated state. The energy of this state can be estimated from electrochemical measurements of the first oxidation and first reduction potentials of **poly2**. The first oxidation potential of **poly2** is at 0.75 Volts vs SCE and the first reduction potential is at -0.63 Volts vs SCE. The difference between these two potentials provides an estimate of the potential energy of this state. Using the maximum current densities calculated previously and this 1.38 eV estimate of the energy of the charge separated state, the maximum open-circuit voltage can be calculated using Equation 3.5. The results of these calculations are shown in Figure 3.32 and indicate that the maximum open-circuit voltage obtainable from these **poly2** films is around 0.9 Volts.

$$V_{max} = \frac{kT}{q} log\left(\frac{J_{max}}{2q\Phi_{cell}(1.38\ eV)}\right) \tag{3.5}$$

The open circuit voltage of an organic solar cell is reduced by the electrostatic energy which binds positive and negative charge carriers together after light absorption. This electrostatic energy was estimated for **poly2** using measurments of the distance between the porphyrin and fullerene in **1**, and a dielectric constant of 4. The measurements of the distance between the porphyrin and fullerene in **1** are between 7 Å and 15 Å. These distances result in electrostatic binding energies between 0.223 eV and 0.452 eV. The differences between the maximum open-circuit voltages in Figure 3.32 and the measured values in Figure 3.31 are at least as large as this estimated electrostatic binding energy. Decreases in the measured values beyond what is accounted for by the electrostatic binding energy are attributed to non-radiative recombination mechanisms.

The affect of light intensity on open-circuit voltage was investigated by measuring I-V curves at five different light intensites. Figure 3.33 shows the results of these measurements on **poly1** films. The value of measurements from sixty spots were

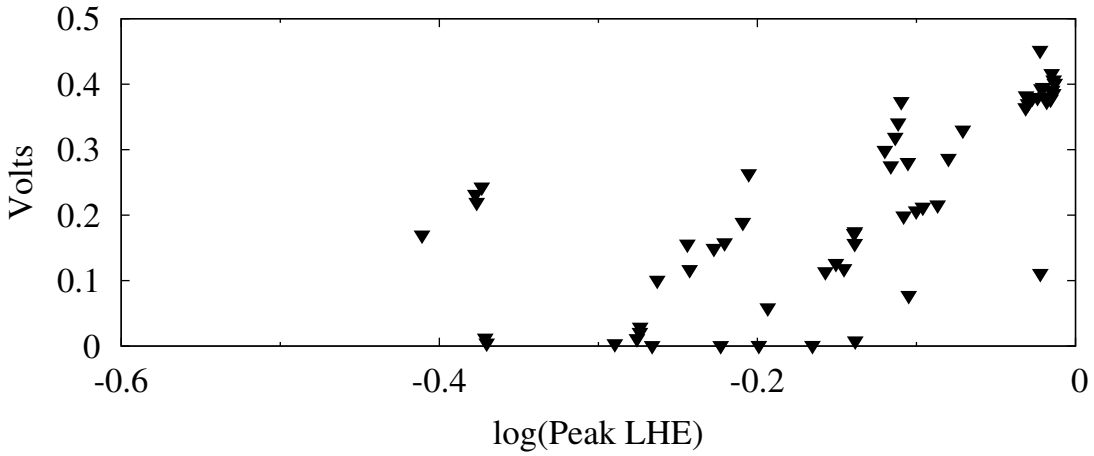

Figure 3.31: Open-circuit voltage from sixty spots tested on **poly2** films under simulated AM1.5G light with an intensity of 100 mW/cm^2.

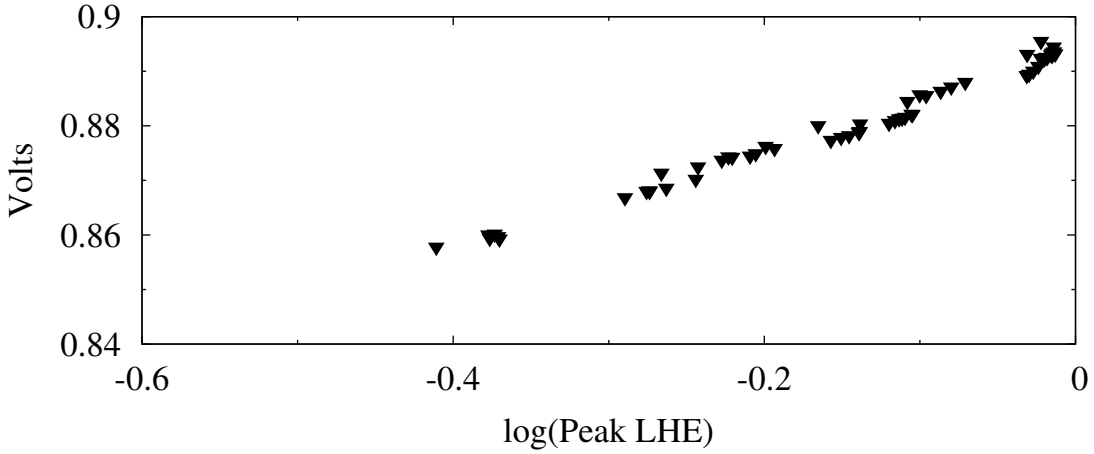

Figure 3.32: Maximum open-circuit voltage possible for all spots on **poly2** films calculated using the LHE spectrum of each spot and the photon flux density of the AM1.5G spectrum.

averaged to produce each data point in the figure. Four of the five data points suggest a linear relationship between light intensity and open-circuit voltage. The data point at 100 mW/cm^2 is from the first I-V curve measurement on each spot. The process of measuring an I-V curve applies a voltage across the film and was observed to change the initial performance of the device. From these measurements, it appears that the greatest change in performance occurs during the first I-V curve measurement. A linear relationship between light intensity and open-circuit voltage indicates that

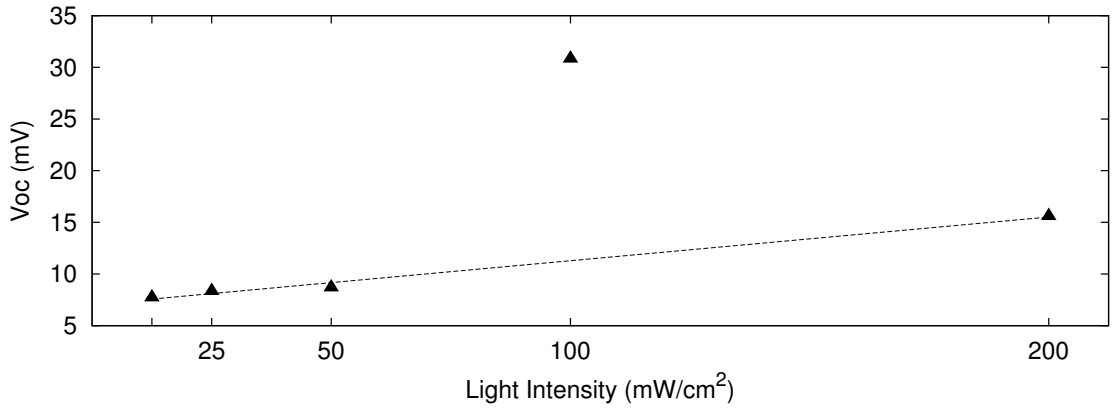

Figure 3.33: Average of sixty open-circuit voltage measurements on **poly1** films at five light intensities.

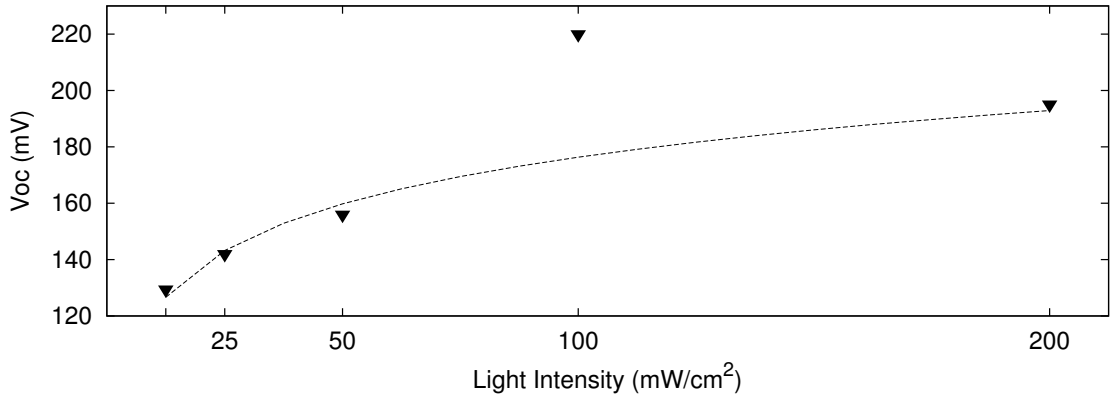

Figure 3.34: Average of sixty open-circuit voltage measurements on **poly2** films at five light intensities.

the voltage of this system is limited by the leakage current through the film. In this situation the resistance of the film establishes a linear relationship between the light-derived current and voltage. Figure 3.28 shows the corresponding results on **poly2** films and for these films the open-circuit voltage increases in proportion to the logarithm of light intensity indicating that the voltage is not limited by leakage current through the film, but instead by the reduced driving force for charge separation at the much higher open-circuit voltages achieved on **poly2** films.

Chapter 4

CONCLUSIONS

The photovoltaic effect was observed in both the porphyrin polymer, **poly1**, and the porphyrin-fullerene polymer, **poly2**, studied here. A means of providing the asymmetry needed for the separation of positive and negative charge carriers is required. Simply polymerizing films of these polymers on ITO or FTO substrates and contacting them with a mercury drop electrode does not produce reliable photocurrents, however treating the surface of the mercury drop with alkanethiols did lead to reliable photocurrents for films of both polymers. Longer alkanethiols resulted in higher photovoltages, but lower photocurrents. Treating the mercury surface with hexanethiol provided the optimum trade-off between photovoltage and photocurrent. The dipole moments of the hexanethiols on the mercury surface reduce the effective work function of the mercury drop. The reduction in work function was estimated to be 0.6 eV using a dipole moment of 1.36 Debye and an area of 20 square Angstroms for each hexanethiol molecule. Despite the sizable difference between electrode work functions, **poly1** did not show appreciable photovoltage until FTO substrates were treated with chlorotrimethylsilane and diisopropylethylamine. This suggests that the FTO-**poly1** interface was an active site for recombination prior to this treatment. Under simulated 100 mW/cm^2 AM1.5G light, short-circuit current measurements on **poly2** films were thirteen-fold larger than those on **poly1**, and the open-circuit voltages were 7-fold larger. The electrostatic energy holding positive and negative charge carriers together in the porphyrin radical cation-fullerene radical anion charge separated state in **poly2** was estimated to be between 223 meV and 452 meV. These estimates are less than the differences between the measured open-

circuit voltage values and the maximum theoretical open-circuit voltages calculated using the Shockley-Queisser method. The linear I-V curves on these polymers suggest high series resistances. However, the logarithmic relationship between V_{OC} and light intensity suggests that if the series resistance could be lowered the I-V curves would be exponential. Incident photon to current efficiency spectra indicate that the dominant photocurrent generation mechanism is located at the mercury interface for both polymers. This severely limits the performance of this system because the light intensity approaches zero at the mercury surface due to the reflection of light at this interface. These polymers may perform well in photovoltaic devices that have structures optimized to take advantage of the optical field distribution within the cells.

REFERENCES

Harnessing Variable Renewables, International Energy Agency, `http://www.iea.org/publications/freepublications/publication/Harnessing_Variable_Renewables2011.pdf` (2011).

FAQ: What is U.S. electricity generation by energy source?, US Energy Information Administration, `http://www.eia.gov/tools/faqs/faq.cfm?id=427&t=3` (2012).

Standard Tables for Reference Solar Spectral Irradiances: Direct Normal and Hemispherical on 37° Tilted Surface, ASTM International (2012).

International energy outlook 2013, US Energy Information Administration, `http://www.eia.gov/forecasts/ieo/pdf/0484(2013).pdf` (2013).

Levelized Cost of New Generation Resources in the Annual Energy Outlook 2013, US Energy Information Administration, `http://www.eia.gov/forecasts/aeo/er/pdf/electricity_generation.pdf` (2013).

Basu, J. and K. Rohatgi-Mukherjee, "Photoelectrochemical characterisation of porphyrin-coated electrodes", Solar Energy Materials **21**, 4, 317 – 325 (1991).

Bedioui, F., J. Devynck and C. Bied-Charreton, "Immobilization of metalloporphyrins in electropolymerized films: design and applications", Accounts of Chemical Research **28**, 1, 30–36 (1995).

Brabec, C., A. Cravino, D. Meissner, N. Sariciftci, T. Fromherz, M. Rispens, L. Sanchez and J. Hummelen, "Origin of the open circuit voltage of plastic solar cells", Advanced Functional Materials **11**, 5, 374–380 (2001).

Carter, S., M. Angelopoulos, S. Karg, P. Brock and J. Scott, "Polymeric anodes for improved polymer light-emitting diode performance", Applied physics letters **70**, 2067–2069 (1997).

Duanmu, C.-S., Z.-P. Chen, X.-S. Yu and X. Zhou, "Synthesis of covalently-linked linear donor-acceptor copolymers containing porphyrins and oligothiophenes", Chinese Journal of Chemistry **22**, 8, 779–781 (2004).

Fish, J. R., E. Kubaszewski, A. Peat, T. Malinski, J. Kaczor, P. Kus and L. Czuchajowski, "Synthesis and electrochemistry of conductive copolymeric porphyrins", Chemistry of Materials **4**, 4, 795–803 (1992).

Fitzner, R., E. Mena-Osteritz, A. Mishra, G. Schulz, E. Reinold, M. Weil, C. Koerner, H. Ziehlke, C. Elschner, K. Leo, M. Riede, M. Pfeiffer, C. Uhrich and P. Baeuerle, "Correlation of pi-Conjugated Oligomer Structure with Film Morphology and Organic Solar Cell Performance", Journal of the American Chemical Society **134**, 27, 11064–11067 (2012).

Gervaldo, M., P. A. Liddell, G. Kodis, B. J. Brennan, C. R. Johnson, J. W. Bridgewater, A. L. Moore, T. A. Moore and D. Gust, "A photo- and electrochemically-active porphyrin-fullerene dyad electropolymer", Photochem. Photobiol. Sci. **9**, 7, 890–900 (2010).

Ghosh, A. K., D. L. Morel, T. Feng, R. F. Shaw and C. A. Rowe, "Photovoltaic and rectification properties of al/mg phthalocyanine/ag schottkybarrier cells", Journal of Applied Physics **45**, 1, 230–236 (1974).

Green, M. A., K. Emery, Y. Hishikawa, W. Warta and E. D. Dunlop, "Solar cell efficiency tables (version 43)", Progress in Photovoltaics: Research and Applications **22**, 1, 1–9 (2014).

Hains, A. W., Z. Liang, M. A. Woodhouse and B. A. Gregg, "Molecular semiconductors in organic photovoltaic cells", Chemical Reviews **110**, 11, 6689–6735 (2010).

Halls, J., K. Pichler, R. Friend, S. Moratti and A. Holmes, "Exciton diffusion and dissociation in a poly(p-phenylenevinylene)/C_{60} heterojunction photovoltaic cell", Applied physics letters **68**, 3120 (1996).

Halls, J., C. Walsh, N. Greenham, E. Marseglia, R. Friend, S. Moratti and A. Holmes, "Efficient photodiodes from interpenetrating polymer networks", Nature **376**, 498–500 (1995).

Haugeneder, A., M. Neges, C. Kallinger, W. Spirkl, U. Lemmer, J. Feldmann, U. Scherf, E. Harth, A. Gügel and K. Müllen, "Exciton diffusion and dissociation in conjugated polymer/fullerene blends and heterostructures", Physical Review B **59**, 23, 15346 (1999).

He, Z., C. Zhong, X. Huang, W.-Y. Wong, H. Wu, L. Chen, S. Su and Y. Cao, "Simultaneous enhancement of open-circuit voltage, short-circuit current density, and fill factor in polymer solar cells", Advanced Materials **23**, 40, 4636–4643 (2011).

Helander, M. G., M. T. Greiner, Z. B. Wang, W. M. Tang and Z. H. Lu, "Work function of fluorine doped tin oxide", Journal of Vacuum Science & Technology A **29**, 1, – (2011).

Hinterwirth, H., S. Kappel, T. Waitz, T. Prohaska, W. Lindner and M. Laemmerhofer, "Quantifying Thiol Ligand Density of Self-Assembled Monolayers on Gold Nanoparticles by Inductively Coupled Plasma-Mass Spectrometry", ACS Nano **7**, 2, 1129–1136 (2013).

Hung, L., C. Tang and M. Mason, "Enhanced electron injection in organic electroluminescence devices using an Al/LiF electrode", Applied Physics Letters **70**, 152–154 (1997).

Jacobson, M. Z. and M. A. Delucchi, "A Path to Sustainable Energy by 2030 (vol 301, pg 58, 2009)", Scientific American **302**, 3, 10 (2010).

Kearns, D. and M. Calvin, "The photovoltaic effect and photoconductivity in laminated organic systems", Journal of Chemical Physics **29**, UCRL–8441 (1958).

Kim, J., S. Kim, H. Lee, K. Lee, W. Ma, X. Gong and A. Heeger, "New architecture for high-efficiency polymer photovoltaic cells using solution-based titanium oxide as an optical spacer", Advanced materials **18**, 5, 572–576 (2006).

Li, G., S. Bhosale, S. Tao, R. Guo, S. Bhosale, F. Li, Y. Zhang, T. Wang and J.-H. Fuhrhop, "Very stable, highly electroactive polymers of zinc(ii)-5,15-bisthienylphenyl porphyrin exhibiting charge-trapping effects", Polymer **46**, 14, 5299 – 5307 (2005).

Liang, Y., Z. Xu, J. Xia, S.-T. Tsai, Y. Wu, G. Li, C. Ray and L. Yu, "For the bright future—bulk heterojunction polymer solar cells with power conversion efficiency of 7.4%", Advanced Materials **22**, 20, E135–E138 (2010).

Liddell, P. A., M. Gervaldo, J. W. Bridgewater, A. E. Keirstead, S. Lin, T. A. Moore, A. L. Moore and D. Gust, "Porphyrin-based hole conducting electropolymer", Chemistry of Materials **20**, 1, 135–142 (2008).

Liu, Y. and H. Yu, "Alkyl monolayer-passivated metal-semiconductor diodes: Molecular tunability and electron transport", ChemPhysChem **3**, 9, 799–802 (2002).

Ma, H., H.-L. Yip, F. Huang and A. K.-Y. Jen, "Interface engineering for organic electronics", Advanced Functional Materials **20**, 9, 1371–1388 (2010).

Mathias, S. and E. D. C. Filho, "The dipole moments of alkanethiols", The Journal of Physical Chemistry **62**, 11, 1427–1430 (1958).

Morel, D., A. Ghosh, T. Feng, E. Stogryn, P. Purwin, R. Shaw and C. Fishman, "High-efficiency organic solar cells", Applied Physics Letters **32**, 8, 495–497 (1978).

Moul, A. J. and K. Meerholz, "Interference method for the determination of the complex refractive index of thin polymer layers", Applied Physics Letters **91**, 6 (2007).

Padinger, F., R. Rittberger and N. Sariciftci, "Effects of postproduction treatment on plastic solar cells", Advanced Functional Materials **13**, 1, 85–88 (2003).

Pettersson, L., L. Roman and O. Inganäs, "Modeling photocurrent action spectra of photovoltaic devices based on organic thin films", Journal of Applied Physics **86**, 487 (1999).

Poriel, C., Y. Ferrand, P. L. Maux, C. Paul-Roth, G. Simonneaux and J. Rault-Berthelot, "Anodic oxidation and physicochemical properties of various porphyrin-fluorenes or -spirobifluorenes: Synthesis of new polymers for heterogeneous catalytic reactions", Journal of Electroanalytical Chemistry **583**, 1, 92 – 103 (2005).

Qin, D., P. Gu, R. S. Dhar, S. G. Razavipour and D. Ban, "Measuring the exciton diffusion length of c60 in organic planar heterojunction solar cells", physica status solidi (a) **208**, 8, 1967–1971 (2011).

Radziszewski, J. G., M. Nepras, V. Balaji, J. Waluk, E. Vogel and J. Michl, "Polarized infrared spectra of photooriented matrix-isolated free-base porphyrin isotopomers", The Journal of Physical Chemistry **99**, 39, 14254–14260 (1995).

Reyes-Reyes, M., K. Kim and D. Carroll, "High-efficiency photovoltaic devices based on annealed poly(3-hexylthiophene) and 1-(3-methoxycarbonyl)-propyl-1-phenyl-(6,6)C_{61} blends", Applied Physics Letters **87**, 083506 (2005).

Savenije, T., J. Warman and A. Goossens, "Visible light sensitisation of titanium dioxide using a phenylene vinylene polymer", Chemical physics letters **287**, 1-2, 148–153 (1998).

Scharber, M., D. Mühlbacher, M. Koppe, P. Denk, C. Waldauf, A. Heeger and C. Brabec, "Design rules for donors in bulk-heterojunction solar cells–Towards 10% energy-conversion efficiency", Advanced Materials **18**, 6, 789–794 (2006).

Shaheen, S., C. Brabec, N. Sariciftci, F. Padinger, T. Fromherz and J. Hummelen, "2.5% efficient organic plastic solar cells", Applied Physics Letters **78**, 841–843 (2001).

Shockley, W. and H. J. Queisser, "Detailed balance limit of efficiency of pn junction solar cells", Journal of Applied Physics **32**, 3, 510–519 (1961).

Tang, C., "Two-layer organic photovoltaic cell", Applied Physics Letters **48**, 2, 183–185 (1986).

Tang, C. and A. Albrecht, "Photovoltaic effects of metal–chlorophyll-a–metal sandwich cells", The Journal of Chemical Physics **62**, 2139 (1975).

Theander, M., A. Yartsev, D. Zigmantas, V. Sundström, W. Mammo, M. Andersson and O. Inganäs, "Photoluminescence quenching at a polythiophene/C_{60} heterojunction", Physical Review B **61**, 19, 12957 (2000).

Wöhrle, D., "Porphyrins, phthalocyanines and related systems in polymer phases", Journal of Porphyrins and Phthalocyanines **4**, 4, 418–424 (2000).

Yip, H.-L., S. K. Hau, N. S. Baek and A. K. Y. Jen, "Self-assembled monolayer modified ZnO/metal bilayer cathodes for polymer/fullerene bulk-heterojunction solar cells", Applied Physics Letters **92**, 19 (2008a).

Yip, H.-L., S. K. Hau, N. S. Baek, H. Ma and A. K.-Y. Jen, "Polymer solar cells that use self-assembled-monolayer- modified zno/metals as cathodes", Advanced Materials **20**, 12, 2376–2382 (2008b).

You, J., L. Dou, K. Yoshimura, T. Kato, K. Ohya, T. Moriarty, K. Emery, C.-C. Chen, J. Gao, G. Li *et al.*, "A polymer tandem solar cell with 10.6% power conversion efficiency", Nature communications **4**, 1446 (2013).

Yu, G. and A. Heeger, "Charge separation and photovoltaic conversion in polymer composites with internal donor/acceptor heterojunctions", Journal of Applied Physics **78**, 7, 4510–4515 (1995).

Zhang, Y.-H., W.-J. Ruan, Z.-Y. Li, Y. Wu and J.-Y. Zheng, "Dft study on the influence of meso-phenyl substitution on the geometric, electronic structure and vibrational spectra of free base porphyrin", Chemical Physics **315**, 12, 201–213 (2005).

Zhou, Y., C. Fuentes-Hernandez, J. Shim, J. Meyer, A. J. Giordano, H. Li, P. Winget, T. Papadopoulos, H. Cheun, J. Kim, M. Fenoll, A. Dindar, W. Haske, E. Najafabadi, T. M. Khan, H. Sojoudi, S. Barlow, S. Graham, J.-L. Brédas, S. R. Marder, A. Kahn and B. Kippelen, "A universal method to produce low–work function electrodes for organic electronics", Science **336**, 6079, 327–332 (2012).

APPENDIX A

GNU OCTAVE CODE

GNU Octave is an open source program that is similar to MATLAB. This appendix contains the Octave code used to perform numerous calculations mentioned in the text.

A.1 Shockley-Queisser Efficiency Limit

```
% script to plot AM1.5G spectrum

% If any arguments are given save figures as files otherwise display them
% on the screen.
if (nargin > 0)
  % Save figures as eps files for conversion to pdf format
  terminal = @(fig,figure_name,x,y) sprintf(["set term postscript eps
      enhanced " \
    "'Times-Roman, 26' size '%f in','%f in';set output
       '%s.eps';"],x,y,figure_name);
else
  % Plot figures on the screen
  terminal = @(fig, figure_name) sprintf('set term wxt %d enhanced;',fig);
end

fig_width = 6;        % width of a full column in ASU dissertations

fig = 1;

% unit conversion constants
m2_to_cm2 = 1e-4;
W_to_mW = 1e3;
mW_to_W = 1e-3;
eV_to_mJ = 1.6e-16;
q = 1.6e-19;          % electronic charge
c = 3e10;             % speed of light (cm/s)
h = 6.626e-34/q;      % planck's constant (eV*s)
k = 1.380e-23/q;      % Boltzman's constant (eV/K)
T = 300;


% read in AM1.5G spectrum (W/m^2)
data = read_datafile('ASTMG173.csv');
wavelength = data(:,1);
energy = 1240./wavelength;
spectral_irradiance = data(:,3)*m2_to_cm2*W_to_mW;


%%%%%%%%%%%%%%%%%%%%%%%%%%%%%%%%%%%%%%%%%%%%%%%%%%%%%%%%%%%%%%%%%%%%%%%%%%%
% plot AM1.5G spectral irradiance (mW cm^-2 nm^-1) vs wavelength
%%%%%%%%%%%%%%%%%%%%%%%%%%%%%%%%%%%%%%%%%%%%%%%%%%%%%%%%%%%%%%%%%%%%%%%%%%%
gnuplot_options = [ terminal(fig++,"AM15G_spectral_irradiance",6,2.5) \
```

```
  "unset title;" \
  "set xlabel 'Wavelength (nm)';" \
  "set xrange [0:4000];" \
  "set xtics nomirror out ('' 0,'500' 500,'' 1000,'1500' 1500,''
     2000,'2500' 2500,'' 3000,'3500' 3500);" \
  "set x2range [0:4000];" \
  "set x2tics nomirror in ('' 0,'' 500,'' 1000,'' 1500,'' 2000,'' 2500,''
     3000,'' 3500);" \
  "set ylabel 'mW cm^{-2} nm^{-1}' offset 1.2;" \
  "set yrange [0:0.18];" \
  "set ytics ('0' 0,'' 0.02,'0.04' 0.04,'' 0.06,'0.08' 0.08,'' 0.1,'0.12'
     0.12,'' 0.14,'0.16' 0.16);" \
  "set key off;" \
];
plot_data([wavelength spectral_irradiance],"with",{"lines lc 0 lw 2"},
  "gnuplot",gnuplot_options)

total_irradiance = trapz(wavelength,spectral_irradiance)

% integration with change of variables dx become (dx/dy)*dy
total_irradiance =
    trapz(energy,-(h*1e7*c)./(energy.^2).*spectral_irradiance)

%%%%%%%%%%%%%%%%%%%%%%%%%%%%%%%%%%%%%%%%%%%%%%%%%%%%%%%%%%%%%%%%%%%%%%%%%%%%
% plot photon flux density of AM1.5G spectrum vs wavelength
%%%%%%%%%%%%%%%%%%%%%%%%%%%%%%%%%%%%%%%%%%%%%%%%%%%%%%%%%%%%%%%%%%%%%%%%%%%%
%"unset xlabel; set xrange [250:4000];" \
photon_flux_density = spectral_irradiance./(1240*eV_to_mJ./wavelength);

total_flux = trapz(wavelength,photon_flux_density)
total_flux = trapz(energy,-(h*1e7*c)./(energy.^2).*photon_flux_density)

gnuplot_options = [ terminal(fig++,"AM15G_photon_flux",6,2.5) \
  "unset title;" \
  "set xlabel 'Wavelength (nm)';" \
  "set ylabel 'Photon Flux (photons cm^{-2} nm^{-1})';" \
  "set key off;" \
];
plot_data([wavelength photon_flux_density],"with",{"lines lc 0 lw 2"},
  "gnuplot",gnuplot_options)


%%%%%%%%%%%%%%%%%%%%%%%%%%%%%%%%%%%%%%%%%%%%%%%%%%%%%%%%%%%%%%%%%%%%%%%%%%%%
% plot AM1.5G spectral photon flux (mW cm^-2 nm^-1) vs photon energy
%%%%%%%%%%%%%%%%%%%%%%%%%%%%%%%%%%%%%%%%%%%%%%%%%%%%%%%%%%%%%%%%%%%%%%%%%%%%

gnuplot_options = [ terminal(fig++,"AM15G_photon_flux_vs_energy",6,2.5) \
  "unset title;" \
  "set xlabel 'Energy (eV)';" \
  "set xrange [0:4.5];" \
```

```
  "set xtics nomirror out ('0' 0,'' 0.5,'1' 1,'' 1.5,'2' 2,'' 2.5,'3' 3,''
     3.5,'4' 4,'' 4.5);" \
  "set x2range [0:4.5];" \
  "set x2tics nomirror in ('' 0,'' 0.5,'' 1,'' 1.5,'' 2,'' 2.5,'' 3,''
     3.5,'' 4,'' 4.5);" \
  "set ylabel 'photons cm^{-2} s^{-1} eV^{-1} x 10^{-17}' offset 0.1;" \
  "set yrange [0:4.5];" \
  "set ytics ('0' 0,'' 0.5,'1' 1,'' 1.5,'2' 2,'' 2.5,'3' 3,'' 3.5,'4' 4);"
     \
  "set key off;" \
];
plot_data([energy
    1e-17*(h*1e7*c)./(energy.^2).*photon_flux_density],"with",{"lines lc 0
    lw 2"},
  "gnuplot",gnuplot_options)


%%%%%%%%%%%%%%%%%%%%%%%%%%%%%%%%%%%%%%%%%%%%%%%%%%%%%%%%%%%%%%%%%%%%%%%%%%%%
% plot maximum current density of AM1.5G spectrum vs wavelength
%%%%%%%%%%%%%%%%%%%%%%%%%%%%%%%%%%%%%%%%%%%%%%%%%%%%%%%%%%%%%%%%%%%%%%%%%%%%

% black body radiation as a function of vg from Shockley1961
%v = energy/h; % photon frequency
%Qc = 2*pi/c^2 * cumtrapz(-v,v.^2./(exp(h*v/(k*T)) - 1));

% took the above and did a change of variables to get it as a function of
    energy
Qc = 2*pi/(h^3*c^2) * cumtrapz(-energy,energy.^2./(exp(energy/(k*T)) - 1));
Jrad0 = 1000*2*q*Qc;
Porphyrin_Polymer_Jrad0 = Jrad0(min(find(energy < 1.8)))
PC60_Polymer_Jrad0 = Jrad0(min(find(energy < 1.38)))

% calculate maximum current density for each wavelenth of absorption onset
Jam15g =
    1000*q*cumtrapz(energy,-(h*1e7*c)./(energy.^2).*photon_flux_density);
Jmax = Jam15g - Jrad0;

total_current_density = 1000*q*trapz(wavelength,photon_flux_density)
total_current_density =
    1000*q*trapz(energy,-(h*1e7*c)./(energy.^2).*photon_flux_density)

% print out value for 1.8 eV so I can use it in the paper
Silicon_Jsc = Jmax(min(find(energy < 1.1)))
Porphyrin_Polymer_Jsc = Jmax(min(find(energy < 1.8)))

%gnuplot_options = [ terminal(fig++,"AM15G_current_density",3,2.5) \
  %"unset title;" \
  %"set xlabel 'Wavelength of absorption onset (nm)';" \
  %"set ylabel 'Maximum Current Density (mA cm^{-2}';" \
  %"set key off;" \
```

```
%];
%plot_data([wavelength Jmax],"with",{"lines lc 0 lw 2"},
  %"gnuplot",gnuplot_options)


%%%%%%%%%%%%%%%%%%%%%%%%%%%%%%%%%%%%%%%%%%%%%%%%%%%%%%%%%%%%%%%%%%%%%%%%%%%%%%%
% plot maximum current density of AM1.5G spectrum vs bandgap
%%%%%%%%%%%%%%%%%%%%%%%%%%%%%%%%%%%%%%%%%%%%%%%%%%%%%%%%%%%%%%%%%%%%%%%%%%%%%%%
gnuplot_options = [ terminal(fig++,"AM15G_MaxJ_vs_Bandgap",6,2.5) \
  "unset title;" \
  "set xlabel 'E_g (eV)';" \
  "set xrange [0:4.5];" \
  "set xtics ('0' 0,'0.5' 0.5,'1' 1,'1.5' 1.5,'2' 2,'2.5' 2.5,'3' 3,'3.5'
     3.5,'4' 4,'4.5' 4.5);" \
  "set ylabel 'J_{max} (mA cm^{-2})' offset 0.5;" \
  "set key off;" \
];
%plot_data([energy Jmax],[energy Jam15g],"with",{"lines lc 0 lw 2","lines
    lc 0 lw 2"},
plot_data([energy Jmax],"with",{"lines lc 0 lw 2"},
  "gnuplot",gnuplot_options)


%%%%%%%%%%%%%%%%%%%%%%%%%%%%%%%%%%%%%%%%%%%%%%%%%%%%%%%%%%%%%%%%%%%%%%%%%%%%%%%
% plot maximum voltage from AM1.5G spectrum vs bandgap
%%%%%%%%%%%%%%%%%%%%%%%%%%%%%%%%%%%%%%%%%%%%%%%%%%%%%%%%%%%%%%%%%%%%%%%%%%%%%%%

% calculation of maximum cell voltage assuming solar generation =
    radiative recombination
Vmax = k*T * log(Jam15g./Jrad0);

% print out value for 1.8 eV so I can use it in the paper
Silicon_Voc = Vmax(min(find(energy < 1.1)))
Porphyrin_Polymer_Voc = Vmax(min(find(energy < 1.8)))

gnuplot_options = [ terminal(fig++,"AM15G_MaxV_vs_Bandgap",3,2.5) \
  "unset title;" \
  "set xlabel 'E_g (eV)';" \
  "set xrange [0:4.5];" \
  "set xtics ('0' 0,'' 0.5,'1' 1,'' 1.5,'2' 2,'' 2.5,'3' 3,'' 3.5,'4' 4,''
     4.5);" \
  "set ylabel 'V_{max} (Volts)' offset 0;" \
  "set yrange [0:4];" \
  "set ytics ('0' 0,'' 0.5,'1' 1,'' 1.5,'2' 2,'' 2.5,'3' 3,'' 3.5,'4' 4);"
     \
  "set key off;" \
];
plot_data([energy Vmax],"with",{"lines lc 0 lw 2"},
  "gnuplot",gnuplot_options)
```

```
gnuplot_options = [ terminal(fig++,"AM15G_MaxV_div_Bandgap",3,2.5) \
  "unset title;" \
  "set xlabel 'E_g (eV)';" \
  "set xrange [0:4.5];" \
  "set xtics ('0' 0,'' 0.5,'1' 1,'' 1.5,'2' 2,'' 2.5,'3' 3,'' 3.5,'4' 4,''
     4.5);" \
  "set ylabel 'Vmax / E_g' offset 1;" \
  "set yrange [0.3:0.95];" \
  "set ytics ('0.3' 0.3,'' 0.35, '0.4' 0.4,'' 0.45, '0.5' 0.5,'' 0.55,
     '0.6' 0.6,'' 0.65,'0.7' 0.7,'' 0.75, '0.8' 0.8,'' 0.85, '0.9' 0.9);" \
  "set key off;" \
];
plot_data([energy Vmax./energy],"with",{"lines lc 0 lw 2"},
  "gnuplot",gnuplot_options)


%%%%%%%%%%%%%%%%%%%%%%%%%%%%%%%%%%%%%%%%%%%%%%%%%%%%%%%%%%%%%%%%%%%%%%%%%%%%
% plot maximum power conversion efficiency vs bandgap
%%%%%%%%%%%%%%%%%%%%%%%%%%%%%%%%%%%%%%%%%%%%%%%%%%%%%%%%%%%%%%%%%%%%%%%%%%%%
max_power_efficiency = zeros(size(energy));
for index = 1:length(energy)
  Eg = energy(index);
  Jsun = Jam15g(index);
  V = 0:0.01:Eg;
  Jrad = Jrad0(index)*exp(V/(k*T));
  J = Jsun - Jrad;
  power = J .* V;
  max_power_efficiency(index) = 100*max(power)/total_irradiance;
endfor

% print out value for 1.8 eV so I can use it in the paper
Silicon_Pmax = max_power_efficiency(min(find(energy < 1.1)))
Porphyrin_Polymer_Pmax = max_power_efficiency(min(find(energy < 1.8)))

gnuplot_options = [ terminal(fig++,"AM15G_MaxPCE_vs_Bandgap",6,2.5) \
  "unset title;" \
  "set xlabel 'E_g (eV)';" \
  "set xrange [0:4.5];" \
  "set xtics ('0' 0,'0.5' 0.5,'1' 1,'1.5' 1.5,'2' 2,'2.5' 2.5,'3' 3,'3.5'
     3.5,'4' 4,'4.5' 4.5);" \
  "set ylabel 'Efficiency (%)' offset 0.5;" \
  "set key off;" \
];
plot_data([energy max_power_efficiency],"with",{"lines lc 0 lw 2"},
  "gnuplot",gnuplot_options)

gnuplot_options = [ terminal(fig++,"AM15G_FF_vs_Bandgap",3,2.5) \
  "unset title;" \
  "set xlabel 'E_g (eV)';" \
  "set ylabel 'Fill Factor';" \
```

```
  "set key off;" \
];
plot_data([energy
    (max_power_efficiency*total_irradiance/100)./(Vmax.*Jmax)],"with",{"lines
    lc 0 lw 2"},
  "gnuplot",gnuplot_options)
```

A.2 IPCE Model

```
% This is a model of ipce spectra for poly1 and poly2 films. It assumes
    that
% only the photons absorbed within a few nanometers of the polymer-mercury
% interface contribute to current.

% If any arguments are given save figures as files otherwise display them
% on the screen.
if (nargin > 0)
  % Save figures as eps files for conversion to pdf format
  terminal = @(fig,figure_name,x,y) sprintf(["set term postscript eps
      enhanced " ...
    "'Times-Roman, 26' size '%f in','%f in';set output
        '%s.eps';"],x,y,figure_name);
    %"size '%f in','%f in';set output '%s.eps';"],x,y,figure_name);
    %"'Helvetica' 20 size '%f in','%f in';set output
        '%s.eps';"],x,y,figure_name);
else
  % Plot figures on the screen
  terminal = @(fig, figure_name) sprintf('set term wxt %d;',fig);
end

fig_width = 6;
fig_height = 2.5;      % just guessing
sample_area = 0.086;   % cm^2
diode_area = 0.086;    % cm^2

uvvis_path =
    '~/Dropbox/ASU/Research/Porphyrin_polymers/Photovoltaics/UV-Vis/2010Aug9/';
electrical_path = '~/Dropbox/ASU/Research/Porphyrin_polymers/Photovoltaics/
  Electrical_characterization/Bridgewater/';

data = read_datafile([uvvis_path "T1_21p5mm.txt"]);
FTOAbs = [data(501:-5:1,1) data(501:-5:1,2)];

fig = 0;

% This is a figure showing IPCE on the left y-axis and LHE on the right for
% a thinner porphyrin polymer sample. The idea is to show that there are
% enough similarities between IPCE and LHE to attribute the photocurrent to
```

```
% the photons absorbed by the polymer.

% Calculate LHE
data = read_datafile([uvvis_path 'P5_31p5mm.txt']);
P5Abs40mm = [data(501:-5:1,1) data(501:-5:1,2)];
P5Abs40mm = [P5Abs40mm(:,1) P5Abs40mm(:,2) - FTOAbs(:,2)];
P5LHE40mm = [P5Abs40mm(:,1) 1 - 10.^(-P5Abs40mm(:,2))];
wr = find((385 <= P5Abs40mm(:,1)) & (P5Abs40mm(:,1) <= 800));

% Calculate IPCE
diode_file = [electrical_path '2010Jun21/diode4128as185mm.txt'];
sample_file = [electrical_path '2010Jun21/P5as40mm185mm.txt'];
P5IPCE40mm = calc_ipce(sample_file,-sample_area,diode_file,diode_area);

% Calculate film thickness from Soret peak
low_wavelength = 380;
high_wavelength = 480;
P5thickness = 101*max(P5Abs40mm(find(P5Abs40mm(:,1) >= low_wavelength &
    P5Abs40mm(:,1) <= high_wavelength),2))

% Calculate absorption coefficients for all wavelengths
P5AC40mm = [P5Abs40mm(:,1) log(10).*P5Abs40mm(:,2)/P5thickness];

% Assume photons absorbed within a short distance of the rear interface
    are all
% collected and calculate the distance for best fit to experimental data
f = @(x)
    x(1)*exp(-P5AC40mm(wr,2)*P5thickness).*(exp(P5AC40mm(wr,2)*x(2))-1) +
    x(3);
Sr = @(x) sum((f(x) - P5IPCE40mm(wr,2)).^2);

x0 = [1.05;1.05;-0.003];
%[x,fval,info,output] = fminbnd(Sr,0,10,options)
[x,fval,info,output] = fminunc(Sr,x0);
x
Sr(x)

St = sum((P5IPCE40mm(wr,2) - mean(P5IPCE40mm(wr,2))).^2);
r_squared = (St - Sr(x))/St

% Calculate IPCE based on best fit model
P5model40mm = [P5AC40mm(wr,1) f(x)];

fig++;
  %"unset title;" ...
gnuplot_options = [ terminal(fig,"PPIPCEMODEL1",fig_width,fig_height) ...
  "set border linewidth 1;" ...
  "set lmargin 6;" ...
  "set rmargin 5;" ...
  "set xlabel 'Wavelength (nm)';" ...
```

```
  "set xrange [385:750];" ...
  "set xtics ('400' 400,'' 450,'500' 500,'' 550,'600' 600,'' 650,'700'
     700);" ...
  "set ylabel 'IPCE x 10^{4}' offset 2.5;" ...
  "set yrange [0:1.1];" ...
  "set ytics nomirror offset 0.5 0,0.2,1;" ...
  "set key at 700,1;" ...
];
key = {"Thin Poly1","model"};
%plot_data(P5IPCE40mm, "y_op","1e2*y", P5model40mm, "y_op","1e2*y",
%"with",{"lines lc 0 lw 2","lines lc 1 lw 2"},
%"gnuplot",gnuplot_options,"key",key)

% This is a figure showing IPCE on the left y-axis and LHE on the right for
% a thicker porphyrin polymer sample. The point of this figure is to show
% that thick films actually reduce the photocurrent in the Soret region,
% suggesting that photocurrent is being generated at the rear interface.

% Calculate LHE
data = read_datafile([uvvis_path 'P9_21p5mm.txt']);
P9Abs30mm = [data(501:-5:1,1) data(501:-5:1,2)];
P9Abs30mm = [P9Abs30mm(:,1) P9Abs30mm(:,2) - FTOAbs(:,2)];
P9LHE30mm = [P9Abs30mm(:,1) 1 - 10.^(-P9Abs30mm(:,2))];

% Calculate film thickness from Soret peak
low_wavelength = 380;
high_wavelength = 480;
P9thickness = 101*max(P9Abs30mm(find(P9Abs30mm(:,1) >= low_wavelength &
    P9Abs30mm(:,1) <= high_wavelength),2))

% Calculate absorption coefficients for all wavelengths
P9AC30mm = [P9Abs30mm(:,1) log(10).*P9Abs30mm(:,2)/P9thickness];

% Calculate IPCE
diode_file = [electrical_path '2010July19/diode4128as186mm.txt'];
sample_file = [electrical_path '2010July19/P9as30mm186mm.txt'];
P9IPCE30mm = calc_ipce(sample_file,-sample_area,diode_file,diode_area);

% Assume photons absorbed within a short distance of the rear interface
    are all
% collected and calculate the distance for best fit to experimental data

%Jnl_TolX = [1e-17; 1e-12; 1e-12];
%Jphoto_TolX = [1e-17; 1e-17];
%TolX = [Jphoto_TolX; Jnl_TolX];
%options = optimset("TolFun",1e-14,"TolX",TolX);
f = @(x)
    x(1)*exp(-P9AC30mm(wr,2)*P9thickness).*(exp(P9AC30mm(wr,2)*x(2))-1) +
    x(3);
Sr = @(x) sum((f(x) - P9IPCE30mm(wr,2)).^2);
```

```
x0 = [1.5;1.5;-0.003];
%[x,fval,info,output] = fminbnd(Sr,0,10,options)
[x,fval,info,output] = fminunc(Sr,x0);
x

St = sum((P9IPCE30mm(wr,2) - mean(P9IPCE30mm(wr,2))).^2);
r_squared = (St - Sr(x))/St

% Calculate IPCE based on best fit model
P9model30mm = [P9AC30mm(wr,1) f(x)];

%%%%%%%%%%%%%%%%%%%%%%%%%%%%%%%%%%%%%%%%%%%%%%%%%%%%%%%%%%%%%%%%%%%%%%%%%%%


fig++;
  %"unset title;" ...
gnuplot_options = [ terminal(fig,"PPIPCEMODEL2",fig_width,fig_height) ...
  "set border linewidth 1;" ...
  "set lmargin 6;" ...
  "set rmargin 5;" ...
  "set xlabel 'Wavelength (nm)';" ...
  "set xrange [385:750];" ...
  "set xtics ('400' 400,'' 450,'500' 500,'' 550,'600' 600,'' 650,'700'
     700);" ...
  "set ylabel 'IPCE x 10^{4}' offset 2.5;" ...
  "set yrange [0:1.8];" ...
  "set ytics offset 0.5 0,0.2,1.6;" ...
  "set key at 700,1.6;" ...
];
key = {"Thick Poly1","model"};
%plot_data(P9IPCE30mm, "y_op","1e2*y", P9model30mm, "y_op","1e2*y",
%"with",{"lines lc 0 lw 3","lines lc 1 lw 3"},
%"gnuplot",gnuplot_options,"key",key)


% This is a figure showing IPCE on the left y-axis and LHE on the right for
% a thinner PC60 polymer sample. The idea is to show that there are
% enough similarities between IPCE and LHE to attribute the photocurrent to
% the photons absorbed by the polymer.

% Calculate LHE
data = read_datafile([uvvis_path 'C2_41p5mm.txt']);
C2Abs50mm = [data(501:-5:1,1) data(501:-5:1,2)];
C2Abs50mm = [C2Abs50mm(:,1) C2Abs50mm(:,2) - FTOAbs(:,2)];
C2LHE50mm = [C2Abs50mm(:,1) 1 - 10.^(-C2Abs50mm(:,2))];

% Calculate IPCE
diode_file = [electrical_path '2010Jun09/diode4128as190mm.txt'];
sample_file = [electrical_path '2010Jun09/C2as50mm190mm.txt'];
```

```
C2IPCE50mm = calc_ipce(sample_file,-sample_area,diode_file,diode_area);

% Calculate film thickness from Soret peak
low_wavelength = 380;
high_wavelength = 480;
C2thickness = 74*max(C2Abs50mm(find(C2Abs50mm(:,1) >= low_wavelength &
    C2Abs50mm(:,1) <= high_wavelength),2))

% Calculate absorption coefficients for all wavelengths
C2AC50mm = [C2Abs50mm(:,1) log(10).*C2Abs50mm(:,2)/C2thickness];

% Assume photons absorbed within a short distance of the rear interface
    are all
% collected and calculate the distance for best fit to experimental data
f = @(x)
    x(1)*exp(-C2AC50mm(wr,2)*C2thickness).*(exp(C2AC50mm(wr,2)*x(2))-1) +
    x(3);
Sr = @(x) sum((f(x) - C2IPCE50mm(wr,2)).^2);

x0 = [22.5;2.5;-0.04];
%[x,fval,info,output] = fminbnd(Sr,0,10,options)
[x,fval,info,output] = fminunc(Sr,x0);
x

St = sum((C2IPCE50mm(wr,2) - mean(C2IPCE50mm(wr,2))).^2);
r_squared = (St - Sr(x))/St

% Calculate IPCE based on best fit model
C2model50mm = [C2AC50mm(wr,1) f(x)];

fig++;
  %"unset title;" ...
gnuplot_options = [ terminal(fig,"PC60IPCEMODEL1",fig_width,fig_height) ...
  "set border linewidth 1;" ...
  "set lmargin 6;" ...
  "set rmargin 5;" ...
  "set xlabel 'Wavelength (nm)';" ...
  "set xrange [385:750];" ...
  "set xtics ('400' 400,'' 450,'500' 500,'' 550,'600' 600,'' 650,'700'
     700);" ...
  "set ylabel 'IPCE x 10^{2}' offset 2.5;" ...
  "set yrange [0:0.9];" ...
  "set ytics nomirror offset 0.5 0,0.1,0.8;" ...
  "set key at 700,0.8;" ...
];
key = {"IPCE","Model"};
plot_data(C2IPCE50mm,C2model50mm,
"with",{"lines lc 0 lw 2","lines lc 0 lw 2"},
"gnuplot",gnuplot_options,"key",key)
```

```
% This is a figure showing IPCE on the left y-axis and LHE on the right for
% a thicker PC60 polymer sample. The point of this figure is to show
% that thick films actually reduce the photocurrent in the Soret region,
% suggesting that photocurrent is being generated at the rear interface.

% Calculate LHE
data = read_datafile([uvvis_path 'C8_46p5mm.txt']);
C8Abs55mm = [data(501:-5:1,1) data(501:-5:1,2)];
C8Abs55mm = [C8Abs55mm(:,1) C8Abs55mm(:,2) - FTOAbs(:,2)];
C8LHE55mm = [C8Abs55mm(:,1) 1 - 10.^(-C8Abs55mm(:,2))];

% Calculate IPCE
diode_file = [electrical_path '2010July15/diode4128as190mm.txt'];
sample_file = [electrical_path '2010July15/C8as55mm190mm.txt'];
C8IPCE55mm = calc_ipce(sample_file,-sample_area,diode_file,diode_area);

% Calculate film thickness from Soret peak
low_wavelength = 380;
high_wavelength = 480;
C8thickness = 74*max(C8Abs55mm(find(C8Abs55mm(:,1) >= low_wavelength &
    C8Abs55mm(:,1) <= high_wavelength),2))

% Calculate absorption coefficients for all wavelengths
C8AC55mm = [C8Abs55mm(:,1) log(10).*C8Abs55mm(:,2)/C8thickness];

% Assume photons absorbed within a short distance of the rear interface
    are all
% collected and calculate the distance for best fit to experimental data
f = @(x)
    x(1)*exp(-C8AC55mm(wr,2)*C8thickness).*(exp(C8AC55mm(wr,2)*x(2))-1) +
    x(3);
Sr = @(x) sum((f(x) - C8IPCE55mm(wr,2)).^2);

x0 = [0.4;66;-0.02];
%[x,fval,info,output] = fminbnd(Sr,0,10,options)
[x,fval,info,output] = fminunc(Sr,x0);
x

St = sum((C8IPCE55mm(wr,2) - mean(C8IPCE55mm(wr,2))).^2);
r_squared = (St - Sr(x))/St

% Calculate IPCE based on best fit model
C8model55mm = [C8AC55mm(wr,1) f(x)];

fig++;
  %"unset title;" ...
gnuplot_options = [ terminal(fig,"PC60IPCEMODEL2",fig_width,fig_height) ...
  "set border linewidth 1;" ...
  "set lmargin 6.5;" ...
  "set rmargin 5;" ...
```

```
  "set xlabel 'Wavelength (nm)';" ...
  "set xrange [385:750];" ...
  "set xtics ('400' 400,'' 450,'500' 500,'' 550,'600' 600,'' 650,'700'
     700);" ...
  "set ylabel 'IPCE x 10^{2}' offset 2.5;" ...
  "set yrange [0:0.15];" ...
  "set ytics nomirror offset 0.5 0,0.05,0.2;" ...
  "set key at 700,0.125;" ...
];
key = {"IPCE","Model"};
plot_data(C8IPCE55mm,C8model55mm,
"with",{"lines lc 0 lw 2","lines lc 0 lw 2"},
"gnuplot",gnuplot_options,"key",key)
```